nature physics

ARTICLES

https://doi.org/10.1038/s41567-021-01478-8

Check for updates

OPEN

Test of lepton universality in beauty-quark decays

LHCb collaboration*

The standard model of particle physics currently provides our best description of fundamental particles and their interactions. The theory predicts that the different charged leptons, the electron, muon and tau, have identical electroweak interaction strengths. Previous measurements have shown that a wide range of particle decays are consistent with this principle of lepton universality. This article presents evidence for the breaking of lepton universality in beauty-quark decays, with a significance of 3.1 standard deviations, based on proton–proton collision data collected with the LHCb detector at CERN's Large Hadron Collider. The measurements are of processes in which a beauty meson transforms into a strange meson with the emission of either an electron and a positron, or a muon and an antimuon. If confirmed by future measurements, this violation of lepton universality would imply physics beyond the standard model, such as a new fundamental interaction between quarks and leptons.

The standard model (SM) of particle physics provides precise predictions for the properties and interactions of fundamental particles, which have been confirmed by numerous experiments since the inception of the model in the 1960s. However, it is clear that the model is incomplete. The SM is unable to explain cosmological observations of the dominance of matter over antimatter, the apparent dark matter content of the Universe, or the patterns seen in the interaction strengths of the particles. Particle physicists have therefore been searching for 'new physics', that is, new particles and interactions that can explain the SM's shortcomings.

One method to search for new physics is to compare measurements of the properties of hadron decays, where hadrons are bound states of quarks, with their SM predictions. Measurable quantities can be predicted precisely in the decays of a charged beauty hadron, B^+, into a charged kaon, K^+, and two charged leptons, $\ell^+\ell^-$. The B^+ hadron contains a beauty antiquark, $\bar{b}$, and the K^+ a strange antiquark, $\bar{s}$, such that at the quark level the decay involves a $\bar{b} \to \bar{s}$ transition. Quantum field theory allows such a process to be mediated by virtual particles that can have a physical mass larger than the energy available in the interaction. In the SM description of such processes, these virtual particles include the electroweak force carriers, the γ, $W^\pm$ and Z^0 bosons, and the top quark (Fig. 1, left). Such decays are highly suppressed[1], and the fraction of B^+ hadrons that decay into this final state (the branching fraction, $\mathcal{B}$) is on the order of 10^6 (ref. [2]).

A distinctive feature of the SM is that the different leptons, electron (e^-), muon (μ^-) and tau (τ^-), have the same interaction strengths. This is known as 'lepton universality'. The only exception to this is due to the Higgs field, since the lepton–Higgs interaction strength gives rise to the differing lepton masses $m_\tau > m_\mu > m_e$. The suppression of $\bar{b} \to \bar{s}$ transitions is understood in terms of the fundamental symmetries on which the SM is built. Conversely, lepton universality is an accidental symmetry of the SM, which is not a consequence of any axiom of the theory. Extensions to the SM that aim to address many of its shortfalls predict new virtual particles that could contribute to $\bar{b} \to \bar{s}$ transitions (Fig. 1, right) and could have non-universal interactions, hence giving branching fractions of $B^+ \to K^+\ell^+\ell^-$ decays with different leptons that differ from the SM predictions. Whenever a process is specified in this paper, the inclusion of the charge-conjugate mode is implied.

Calculation of the SM predictions for the branching fractions of $B^+ \to K^+\mu^+\mu^-$ and $B^+ \to K^+e^+e^-$ decays is complicated by the strong nuclear force that binds together the quarks into hadrons, as described by quantum chromodynamics (QCD). The large interaction strengths preclude predictions of QCD effects with the perturbation techniques used to compute the electroweak force amplitudes, and only approximate calculations are currently possible. However, the strong force does not couple directly to leptons, hence its effect on the $B^+ \to K^+\mu^+\mu^-$ and $B^+ \to K^+e^+e^-$ decays is identical. The ratio between the branching fractions of these decays is therefore predicted with $\mathcal{O}(1\%)$ precision[3–8]. Due to the small masses of both electrons and muons compared with that of b quarks, this ratio is predicted to be close to unity, except where the value of the dilepton invariant mass-squared (q^2) significantly restricts the phase space available to form the two leptons. Similar considerations apply to decays with other B hadrons, $B \to H\mu^+\mu^-$ and $B \to He^+e^-$, where $B = B^+, B^0, B_s^0$ or Λ_b^0, and H can be, for example, an excited kaon, K^{*0}, or a combination of particles such as a proton and charged kaon, pK^-. The ratio of branching fractions, R_H (refs. [9,10]), is defined in the dilepton mass-squared range $q^2_{\min} < q^2 < q^2_{\max}$ as

$$R_H \equiv \frac{\int_{q^2_{\min}}^{q^2_{\max}} \frac{d\mathcal{B}\ (B \to H\mu^+\mu^-)}{dq^2} dq^2}{\int_{q^2_{\min}}^{q^2_{\max}} \frac{d\mathcal{B}\ (B \to He^+e^-)}{dq^2} dq^2}. \quad (1)$$

For decays with $H = K^+$ and $H = K^{*0}$ such ratios, denoted by R_K and $R_{K^{*0}}$, respectively, have previously been measured by the Large Hadron Collider beauty (LHCb)[11,12], Belle[13,14] and BaBar[15] collaborations. For R_K the LHCb measurements are in the range $1.1 < q^2 < 6.0\,\text{GeV}^2\ c^{-4}$, whereas for $R_{K^{*0}}$, the ranges are $0.045 < q^2 < 1.1\,\text{GeV}^2\ c^{-4}$ and $1.1 < q^2 < 6.0\,\text{GeV}^2\ c^{-4}$. These ratios have been determined to be 2.1–2.5 standard deviations below their respective SM expectations[3–7,16–22]. The analogous ratio has also been measured for Λ_b^0 decays with $H = pK^-$ and is compatible with unity at the level of one standard deviation[23].

These decays all proceed via the same $\bar{b} \to \bar{s}$ quark transition, and the results have therefore further increased interest in measurements of angular observables[24–34] and branching fractions[35–38] of decays mediated by $\bar{b} \to \bar{s}\mu^+\mu^-$ transitions. Such decays also exhibit some tension with the SM predictions but the extent of residual QCD effects is still the subject of debate[3,21,39–47]. A consistent model-independent interpretation of all these data is possible via a modification of the $\bar{b} \to \bar{s}$ coupling strength[48–54]. Such a modification

*A list of authors and their affiliations appears online.

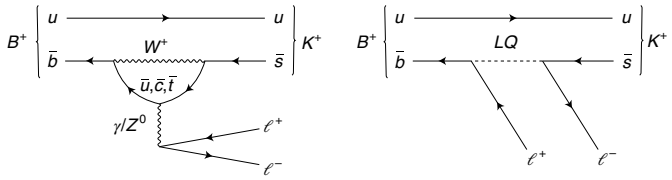

Fig. 1 | Contributions to $B^+ \to K^+\ell^+\ell^-$ decays in the SM and possible new physics models. A B^+ meson, consisting of $\bar{b}$ and u quarks, decays into a K^+, containing $\bar{s}$ and u quarks, and two charged leptons, $\ell^+\ell^-$. Left: the SM contribution involves the electroweak bosons γ, W^+ and Z^0, and the up-type quarks $\bar{u}$, $\bar{c}$ and $\bar{t}$. Right: a possible new physics contribution to the decay with a hypothetical leptoquark (LQ) which, unlike the electroweak bosons, could have different interaction strengths with the different types of leptons.

can be realized in new physics models with an additional heavy neutral boson or with leptoquarks. Other explanations of the data involve a variety of extensions to the SM, such as supersymmetry, extended Higgs–boson sectors and models with extra dimensions. References to the extensive literature describing these new physics models can be found in the Supplementary Information. Tension with the SM is also seen in the combination of several ratios that test lepton universality in $\bar{b} \to \bar{c}\ell^+\nu_\ell$ transitions[55–63].

In this paper, a measurement of the R_K ratio is presented based on proton–proton collision data collected with the LHCb detector at the CERN's Large Hadron Collider (Methods). The data were recorded during 2011, 2012 and 2015–2018 with centre-of-mass energy of the collisions of 7, 8 and 13 TeV and correspond to an integrated luminosity of 9 fb^{-1}. Compared with the previous LHCb R_K result[11], the experimental method is essentially identical but the analysis uses an additional 4 fb^{-1} of data collected in 2017 and 2018. The results supersede those of the previous LHCb analysis.

The analysis strategy aims to reduce systematic uncertainties induced in modelling the markedly different reconstruction of decays with muons in the final state, compared with decays with electrons. These differences arise due to the significant bremsstrahlung radiation emitted by the electrons and the different detector subsystems that are used to identify electron and muon candidates (Methods). The major challenge of the measurement is then correcting for the efficiency of the selection requirements used to isolate signal candidates and reduce background. To avoid unconscious bias, the analysis procedure was developed and the cross-checks described below performed before the result for R_K was examined.

In addition to the process discussed above, the $K^+\ell^+\ell^-$ final state is produced via a $B^+ \to X_{q\bar{q}}K^+$ decay, where $X_{q\bar{q}}$ is a bound state (meson) such as the J/ψ. The J/ψ meson consists of a charm quark and antiquark, $c\bar{c}$, and is produced resonantly at $q^2 = 9.59\,\text{GeV}^2c^{-4}$. This 'charmonium' resonance subsequently decays into two leptons, $J/\psi \to \ell^+\ell^-$. The $B^+ \to J/\psi(\to \ell^+\ell^-)K^+$ decays are not suppressed and hence have a branching fraction orders of magnitude larger than that of $B^+ \to K^+\ell^+\ell^-$ decays. These two processes are separated by applying a requirement on q^2. The $1.1 < q^2 < 6.0\,\text{GeV}^2\,c^{-4}$ region used to select $B^+ \to K^+\ell^+\ell^-$ decays is chosen to reduce the pollution from the J/ψ resonance and the high-q^2 region that contains contributions from further excited charmonium resonances, such as the $\psi(2S)$ and $\psi(3770)$ states, and from lighter $s\bar{s}$ resonances, such as the $\phi(1020)$ meson. In the remainder of this paper, the notation $B^+ \to K^+\ell^+\ell^-$ is used to denote only decays with $1.1 < q^2 < 6.0\,\text{GeV}^2\,c^{-4}$, which are referred to as non-resonant, whereas $B^+ \to J/\psi(\to \ell^+\ell^-)K^+$ decays are denoted resonant.

To help overcome the challenge of modelling precisely the different electron and muon reconstruction efficiencies, the branching fractions of $B^+ \to K^+\ell^+\ell^-$ decays are measured relative to those of $B^+ \to J/\psi K^+$ decays[64]. Since the $J/\psi \to \ell^+\ell^-$ branching fractions are known to respect lepton universality to within 0.4% (refs. [2,65]), the R_K ratio is determined via the double ratio of branching fractions

$$R_K = \frac{\mathcal{B}\,(B^+ \to K^+\mu^+\mu^-)}{\mathcal{B}\,(B^+ \to J/\psi(\to \mu^+\mu^-)K^+)} \Big/ \frac{\mathcal{B}\,(B^+ \to K^+e^+e^-)}{\mathcal{B}\,(B^+ \to J/\psi(\to e^+e^-)K^+)}. \quad (2)$$

In this equation, each branching fraction can be replaced by the corresponding event yield divided by the appropriate overall detection efficiency (Methods), as all other factors needed to determine each branching fraction individually cancel out. The efficiency of the non-resonant $B^+ \to K^+e^+e^-$ decay therefore needs to be known only relative to that of the resonant $B^+ \to J/\psi(\to e^+e^-)K^+$ decay, rather than relative to the $B^+ \to K^+\mu^+\mu^-$ decay. As the detector signature of each resonant decay is similar to that of its corresponding non-resonant decay, systematic uncertainties that would otherwise dominate the calculation of these efficiencies are suppressed. The yields observed in these four decay modes and the ratios of efficiencies determined from simulated events then enable an R_K measurement with statistically dominated uncertainties. As detailed below, percent-level control of the efficiencies is verified with a direct comparison of the $B^+ \to J/\psi(\to e^+e^-)K^+$ and $B^+ \to J/\psi(\to \mu^+\mu^-)K^+$ branching fractions in the ratio

$$r_{J/\psi} = \mathcal{B}\,(B^+ \to J/\psi(\to \mu^+\mu^-)K^+)/\mathcal{B}\,(B^+ \to J/\psi(\to e^+e^-)K^+),$$

which does not benefit from the same cancellation of systematic effects.

Candidate $B^+ \to K^+\ell^+\ell^-$ decays are found by combining the reconstructed trajectory (track) of a particle identified as a charged kaon, together with the tracks from a pair of well-reconstructed oppositely charged particles identified as either electrons or muons. The particles are required to originate from a common vertex, displaced from the proton–proton interaction point, with good vertex-fit quality. The techniques used to identify the different particles and to form B^+ candidates are described in Methods.

The invariant mass of the final state particles, $m(K^+\ell^+\ell^-)$, is used to discriminate between signal and background contributions, with the signal expected to accumulate around the known mass of the B^+ meson. Background originates from particles selected from multiple hadron decays, referred to as combinatorial background, and from specific decays of B hadrons. The latter also tend to accumulate around specific values of $m(K^+\ell^+\ell^-)$. For the muon modes, the residual background is combinatorial and, for the resonant mode, there is an additional contribution from $B^+ \to J/\psi\pi^+$ decays with a pion misidentified as a kaon. For the electron modes, in addition to combinatorial background, other specific background decays contribute significantly in the signal region. The dominant such background for the non-resonant and resonant modes comes from partially reconstructed $B^{(0,+)} \to K^+\pi^{(-,0)}e^+e^-$ and $B^{(0,+)} \to J/\psi(\to e^+e^-)K^+\pi^{(-,0)}$ decays, respectively, where the pion is not included in the B^+ candidate. Decays of the form $B^+ \to \overline{D}{}^0(\to K^+e^-\bar{\nu}_e)e^+\nu_e$ also contribute at the level of $\mathcal{O}(1\%)$ of the $B^+ \to K^+e^+e^-$ signal; and there is also a contribution from $B^+ \to J/\psi(\to e^+e^-)K^+$ decays, where a photon is emitted but not reconstructed. The kinematic correlation between $m(K^+e^+e^-)$ and q^2 means that, irrespective of misreconstruction effects, the latter background can only populate the $m(K^+e^+e^-)$ region well below the signal peak.

After the application of the selection requirements, the resonant and non-resonant decays are clearly visible in the mass distributions (Fig. 2). The yields in the two $B^+ \to K^+\ell^+\ell^-$ and two $B^+ \to J/\psi(\to \ell^+\ell^-)K^+$ decay modes are determined by performing unbinned extended maximum-likelihood fits to these distributions (Methods). For the non-resonant candidates, the $m(K^+e^+e^-)$ and $m(K^+\mu^+\mu^-)$ distributions are fitted with a likelihood function that

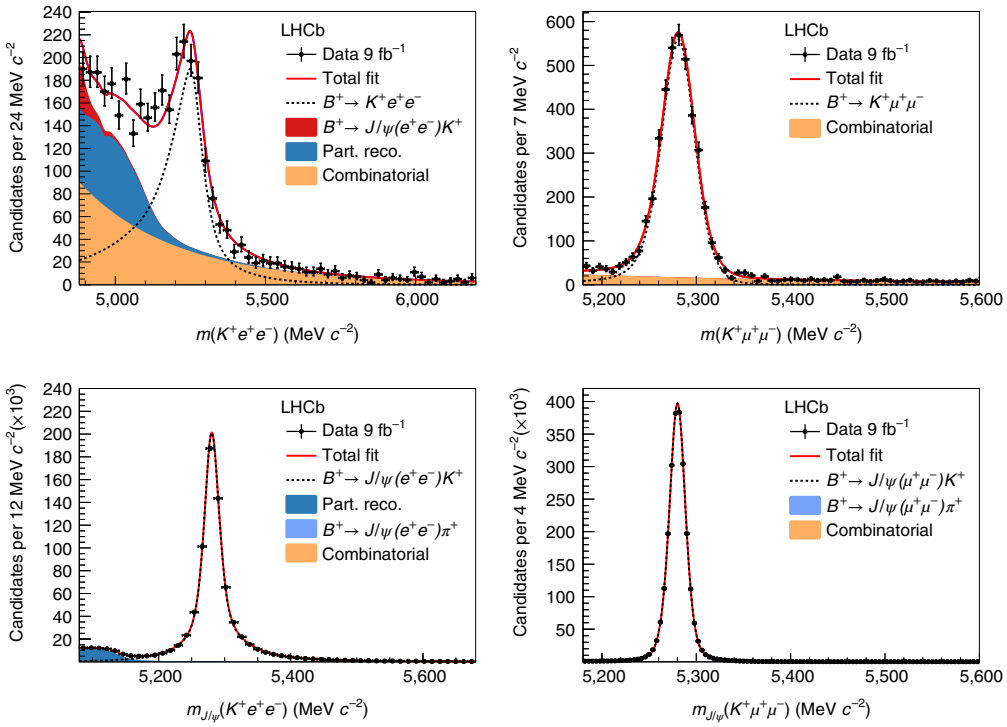

Fig. 2 | Candidate invariant mass distributions. Distribution of the invariant mass $m_{(J/\psi)}(K^+\ell^+\ell^-)$ for candidates with electron (left) and muon (right) pairs in the final state for the non-resonant $B^+ \to K^+\ell^+\ell^-$ signal channels (top) and resonant $B^+ \to J/\psi(\to \ell^+\ell^-)K^+$ decays (bottom). The fit projection is superimposed, with dotted lines describing the signal contribution and solid areas representing each of the background components described in the text and listed in the legend. Part. reco. refers to partially reconstructed B hadron decays. In the resonant-mode distributions, some fit components are too small to be visible. Uncertainties on the data points are statistical only and represent one standard deviation, calculated assuming Poisson-distributed entries. The y axis in each panel shows the number of candidates in an interval of the indicated width.

has the $B^+ \to K^+\mu^+\mu^-$ yield and R_K as fit parameters and the resonant decay mode yields incorporated as Gaussian-constraint terms. The resonant yields are determined from separate fits to the mass, $m_{J/\psi}(K^+\ell^+\ell^-)$, formed by kinematically constraining the dilepton system to the known J/ψ mass[2] and thereby improving the mass resolution.

Simulated events are used to derive the two ratios of efficiencies needed to form R_K using equation (2). Control channels are used to calibrate the simulation to correct for the imperfect modelling of the B^+ production kinematics and various aspects of the detector response. The overall effect of these corrections on the measured value of R_K is a relative shift of $(+3 \pm 1)\%$. When compared with the 20% shift that these corrections induce in the measurement of $r_{J/\psi}$, this demonstrates the robustness of the double-ratio method in suppressing systematic biases that affect the resonant and non-resonant decay modes similarly.

The systematic uncertainty (Methods) from the choice of signal and background mass-shape models in the fits is estimated by fitting pseudo-experiments with alternative models that still describe the data well. The effect on R_K is at the 1% level. A comparable uncertainty arises from the limited size of the calibration samples, with negligible contributions from the calibration of the B^+ production kinematics and modelling of the selection and particle-identification efficiencies. Systematic uncertainties that affect the ratios of efficiencies influence the measured value of R_K and are taken into account using constraints on the efficiency values. Correlations between different categories of selected events and data-taking periods are taken into account in these constraints. The combined statistical and systematic uncertainty is then determined by scanning the profile likelihood, and the statistical contribution to the uncertainty is isolated by repeating the scan with the efficiencies fixed to their fitted values.

The determination of the $r_{J/\psi}$ ratio requires control of the relative selection efficiencies for the resonant electron and muon modes and does not therefore benefit from the cancellation of systematic effects in the double ratio used to measure R_K. Given the scale of the corrections required, comparison of $r_{J/\psi}$ with unity is a stringent cross-check of the experimental procedure. In addition, if the simulation is correctly calibrated, the measured $r_{J/\psi}$ value will not depend on any variable. The $r_{J/\psi}$ ratio is therefore also computed as a function of different kinematic variables. Even though the non-resonant and resonant samples are mutually exclusive as a function of q^2, there is significant overlap between them in the quantities on which the efficiency depends, such as the laboratory-frame momenta of the final-state particles or the opening angle between the two leptons. This is because a given set of values for the final-state particles' momenta and angles in the B^+ rest frame will result in a distribution of such values when transformed to the laboratory frame.

The value of $r_{J/\psi}$ is measured to be 0.981 ± 0.020. This uncertainty includes both statistical and systematic effects, where the latter dominate. The consistency of this ratio with unity demonstrates control of the efficiencies well in excess of that needed for the determination of R_K. In the measurement of the $r_{J/\psi}$ ratio, the systematic uncertainty is dominated by the imperfect modelling of the B^+ production kinematics and the modelling of selection requirements, which have a negligible impact on the R_K measurement. No significant trend is observed in the differential determination of $r_{J/\psi}$ as a function of any considered variable. An example distribution, with $r_{J/\psi}$ determined as a function of B^+ momentum component transverse to the beam direction, p_T, is shown in Fig. 3. Assuming that the observed $r_{J/\psi}$ variation in such distributions reflects genuine mis-modelling of the efficiencies, rather than statistical fluctuations, and taking into account the spectrum of the relevant variables in the non-resonant

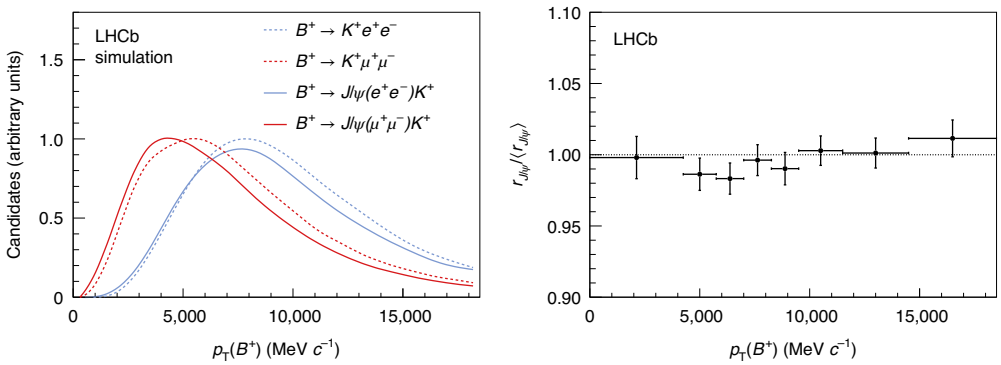

Fig. 3 | Differential $r_{J/\psi}$ measurement. The distributions of the B^+ transverse momentum (p_T, left) and the ratio $r_{J/\psi}$ (right) relative to its average value $< r_{J/\psi} >$ as a function of p_T. The p_T spectrum of the $B^+ \to J/\psi K^+$ decays is similar to that of the corresponding $B^+ \to K^+\ell^+\ell^-$ decays such that the measurement of $r_{J/\psi}$ tests the kinematic region relevant for the R_K measurement. The lack of any dependence of the value of $r_{J/\psi}/ < r_{J/\psi} >$ as a function of B^+ p_T demonstrates control of the efficiencies. Uncertainties on the data points are statistical only and represent one standard deviation.

decay modes, a total shift on R_K is computed for each of the variables examined. The resulting variations are typically at the permille level and hence well within the estimated systematic uncertainty on R_K. Similarly, computations of the $r_{J/\psi}$ ratio in bins of two kinematic variables also do not show any trend and are consistent with the systematic uncertainties assigned on the R_K measurement.

In addition to $B^+ \to J/\psi K^+$ decays, clear signals are observed from $B^+ \to \psi(2S)K^+$ decays. The double ratio of branching fractions, $R_{\psi(2S)}$, defined by

$$R_{\psi(2S)} = \frac{\mathcal{B}(B^+ \to \psi(2S)(\to \mu^+\mu^-)K^+)}{\mathcal{B}(B^+ \to J/\psi(\to \mu^+\mu^-)K^+)} \Big/ \frac{\mathcal{B}(B^+ \to \psi(2S)(\to e^+e^-)K^+)}{\mathcal{B}(B^+ \to J/\psi(\to e^+e^-)K^+)}, \quad (3)$$

provides an independent validation of the double-ratio analysis procedure and further tests the control of the efficiencies. This double ratio is expected to be close to unity[2] and is determined to be 0.997 ± 0.011, where the uncertainty includes both statistical and systematic effects, the former of which dominates. This can be interpreted as a world-leading test of lepton flavour universality in $\psi(2S) \to \ell^+\ell^-$ decays.

The fit projections for the $m(K^+\ell^+\ell^-)$ and $m_{J/\psi}(K^+\ell^+\ell^-)$ distributions are shown in Fig. 2. The fit is of good quality, and the value of R_K is measured to be

$$R_K(1.1 < q^2 < 6.0\,\mathrm{GeV}^2\,c^{-4}) = 0.846^{+0.042+0.013}_{-0.039-0.012},$$

where the first uncertainty is statistical and the second systematic. Combining the uncertainties gives $R_K = 0.846^{+0.044}_{-0.041}$. This is the most precise measurement to date and is consistent with the SM expectation, 1.00 ± 0.01 (refs. [3–7]), at the level of 0.10% (3.1 standard deviations), giving evidence for the violation of lepton universality in these decays. The value of R_K is found to be consistent in subsets of the data divided on the basis of data-taking period, different selection categories and magnet polarity (Methods). The profile likelihood is given in Methods. A comparison with previous measurements is shown in Fig. 4.

The $3{,}850 \pm 70$ $B^+ \to K^+\mu^+\mu^-$ decay candidates that are observed are used to compute the $B^+ \to K^+\mu^+\mu^-$ branching fraction as a function of q^2. The results are consistent between the different data-taking periods and with previous LHCb measurements[37]. The $B^+ \to K^+e^+e^-$ branching fraction is determined by combining the value of R_K with the value of $\mathrm{d}\mathcal{B}(B^+ \to K^+\mu^+\mu^-)/\mathrm{d}q^2$ in the region $1.1 < q^2 < 6.0\,\mathrm{GeV}^2\,c^{-4}$ (ref. [37]), taking into account correlated systematic uncertainties. This gives

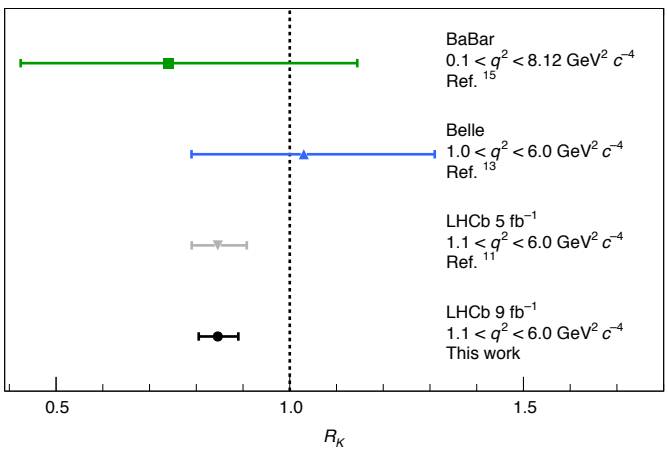

Fig. 4 | Comparison between R_K measurements. In addition to the LHCb result, the measurements by the BaBar[15] and Belle[13] collaborations, which combine $B^+ \to K^+\ell^+\ell^-$ and $B^0 \to K^0_S\ell^+\ell^-$ decays, are also shown. The vertical dashed line indicates the SM prediction. Uncertainties on the data points are the combination of statistical and systematic and represent one standard deviation.

$$\frac{\mathrm{d}\mathcal{B}(B^+ \to K^+e^+e^-)}{\mathrm{d}q^2}(1.1 < q^2 < 6.0\,\mathrm{GeV}^2c^{-4}) = (28.6\,^{+\,1.5}_{-\,1.4} \pm 1.3) \times 10^{-9}\,c^4\,\mathrm{GeV}^{-2}.$$

The 1.9% uncertainty on the $B^+ \to J/\psi K^+$ branching fraction[2] gives rise to the dominant systematic uncertainty. This is the most precise measurement of this quantity to date and, given the large ($\mathcal{O}(10\%)$) theoretical uncertainty on the predictions[7,66], is consistent with the SM.

A breaking of lepton universality would require an extension of the gauge structure of the SM that gives rise to the known fundamental forces. It would therefore constitute a significant evolution in our understanding and would challenge an inference based on a wealth of experimental data in other processes. Confirmation of any effect beyond the SM will clearly require independent evidence from a wide range of sources.

Measurements of other R_H observables with the full LHCb dataset will provide further information on the quark-level processes measured. In addition to affecting the decay rates, new physics can

also alter how the decay products are distributed in phase space. An angular analysis of the electron mode, where SM-like behaviour might be expected in the light of the present results and those from $\overline{b} \to \overline{s}\mu^+\mu^-$ decays, would allow the formation of ratios between observable quantities other than branching fractions, enabling further precise tests of lepton universality[16,18,31,67,68]. The hierarchical effect needed to explain the existing $\overline{b} \to \overline{s}\ell^+\ell^-$ and $\overline{b} \to \overline{c}\ell^+\nu_\ell$ data, with the largest effects observed in tau modes, then muon modes and little or no effects in electron modes, suggests that studies of $\overline{b} \to \overline{s}\tau^+\tau^-$ transitions are also of great interest[69,70]. There are excellent prospects for all of the above and further measurements with the much larger samples that will be collected with the upgraded LHCb detector from 2022 and, in the longer term, with the LHCb Upgrade II[71]. Other experiments should also be able to determine R_H ratios, with the Belle II experiment in particular expected to have competitive sensitivity[72]. The ATLAS and CMS experiments may also be able to contribute[73,74].

In summary, in the dilepton mass-squared region $1.1 < q^2 < 6.0\,\mathrm{GeV}^2c^{-4}$, the ratio of branching fractions for $B^+ \to K^+\mu^+\mu^-$ and $B^+ \to K^+e^+e^-$ decays is measured to be $R_K = 0.846^{+\,0.044}_{-\,0.041}$. This is the most precise measurement of this ratio to date and is compatible with the SM prediction with a P value of 0.10%. The significance of this discrepancy is 3.1 standard deviations, giving evidence for the violation of lepton universality in these decays.

Online content

Any methods, additional references, Nature Research reporting summaries, source data, extended data, supplementary information, acknowledgements, peer review information; details of author contributions and competing interests; and statements of data and code availability are available at https://doi.org/10.1038/s41567-021-01478-8.

Received: 22 March 2021; Accepted: 30 November 2021;
Published online: 15 March 2022

References

1. Glashow, S. L., Iliopoulos, J. & Maiani, L. Weak interactions with lepton–hadron symmetry. *Phys. Rev. D* **2**, 1285–1292 (1970).
2. Particle Data Group et al. Review of particle physics. *Prog. Theor. Exp. Phys.* **2020**, 083C01 (2020).
3. Descotes-Genon, S., Hofer, L., Matias, J. & Virto, J. Global analysis of $b \to s\ell\ell$ anomalies. *J. High. Energy Phys.* **06**, 092 (2016).
4. Bobeth, C., Hiller, G. & Piranishvili, G. Angular distributions of $\bar{B} \to K\bar{\ell}\ell$ decays. *J. High. Energy Phys.* **12**, 040 (2007).
5. Bordone, M., Isidori, G. & Pattori, A. On the standard model predictions for R_K and R_{K^*}. *Eur. Phys. J.* **C76**, 440 (2016).
6. van Dyk, D et al. EOS version 0.3.3. *Zenodo* https://doi.org/10.5281/zenodo.4586379 (2021).
7. Straub, D. M. flavio: a python package for flavour and precision phenomenology in the standard model and beyond. *Zenodo* https://doi.org/10.5281/zenodo.4587748
8. Isidori, G., Nabeebaccus, S. & Zwicky, R. QED corrections in $\overline{B} \to \overline{K}\ell^+\ell^-$ at the double-differential level. *J. High. Energy Phys.* **12**, 104 (2020).
9. Hiller, G. & Krüger, F. More model-independent analysis of $b \to s$ processes. *Phys. Rev. D* **69**, 074020 (2004).
10. Wang, Y. & Atwood, D. Rate difference between $b \to s\mu^+\mu^-$ and $b \to se^+e^-$ in supersymmetry with large tan β. *Phys. Rev. D* **68**, 094016 (2003).
11. Aaij, R. et al. Search for lepton-universality violation in $B^+ \to K^+\ell^+\ell^-$ decays. *Phys. Rev. Lett.* **122**, 191801 (2019).
12. The LHCb collaboration et al. Test of lepton universality with $B^0 \to K^{*0}\ell^+\ell^-$ decays. *J. High Energy Phys.* **2017**, 055 (2017).
13. The Belle collaboration et al. Test of lepton flavor universality and search for lepton flavor violation in $B \to K\ell\ell$ decays. *J. High Energy Phys.* **2021**, 105 (2021).
14. Wehle, S. et al. Test of lepton-flavor universality in $B \to K^*\ell^+\ell^-$ decays at Belle. *Phys. Rev. Lett.* **126**, 161801 (2021).
15. Lees, J. P. et al. Measurement of branching fractions and rate asymmetries in the rare decays $B \to K^{(*)}\ell^+\ell^-$. *Phys. Rev. D* **86**, 032012 (2012).
16. Capdevila, B., Descotes-Genon, S., Matias, J. & Virto, J. Assessing lepton-flavour non-universality from $B \to K\ell\ell$ angular analyses. *J. High. Energy Phys.* **10**, 075 (2016).
17. Capdevila, B., Descotes-Genon, S., Hofer, L. & Matias, J. Hadronic uncertainties in $B \to K\mu^+\mu^-$: a state-of-the-art analysis. *J. High. Energy Phys.* **04**, 016 (2017).
18. Serra, N., Silva Coutinho, R. & van Dyk, D. Measuring the breaking of lepton flavor universality in $B \to K^*\ell^+\ell^-$. *Phys. Rev. D* **95**, 035029 (2017).
19. Bharucha, A., Straub, D. M. & Zwicky, R. $B \to V\ell^+\ell^-$ in the standard model from light-cone sum rules. *J. High. Energy Phys.* **08**, 098 (2016).
20. Altmannshofer, W., Niehoff, C., Stangl, P. & Straub, D. M. Status of the $B \to K^*\mu^+\mu^-$ anomaly after Moriond 2017. *Eur. Phys. J.* **C77**, 377 (2017).
21. Jäger, S. & Martin Camalich, J. Reassessing the discovery potential of the $B \to K^*\ell^+\ell^-$ decays in the large-recoil region: SM challenges and BSM opportunities. *Phys. Rev. D* **93**, 014028 (2016).
22. Ghosh, D., Nardecchia, M. & Renner, S. A. Hint of lepton flavour non-universality in B meson decays. *J. High. Energy Phys.* **12**, 131 (2014).
23. The LHCb collaboration et al. Test of lepton universality using $\Lambda_b^0 \to pK^-\ell^+\ell^-$ decays. *J. High Energy Phys.* **2020**, 40 (2020).
24. Aaij, R. et al. Angular analysis of the $B^+ \to K^{*+}\mu^+\mu^-$ decay. *Phys. Rev. Lett.* **126**, 161802 (2021).
25. Aaij, R. et al. Measurement of *CP*-averaged observables in the $B^0 \to K^{*0}\mu^+\mu_-$ decay. *Phys. Rev. Lett.* **125**, 011802 (2020).
26. The LHCb collaboration et al. Angular analysis of the $B^0 \to K^{*0}\mu^+\mu_-$ decay using 3 fb^{-1} of integrated luminosity. *J. High Energy Phys.* **2016**, 104 (2016).
27. The ATLAS collaboration et al. Angular analysis of $B_d^0 \to K^*\mu^+\mu^-$ decays in pp collisions at $\sqrt{s} = 8$ TeV with the ATLAS detector. *J. High Energy Phys.* **2018**, 47 (2018).
28. Aubert, B. et al. Measurements of branching fractions, rate asymmetries, and angular distributions in the rare decays $B \to K\ell^+\ell^-$ and $B \to K^*\ell^+\ell^-$. *Phys. Rev. D* **73**, 092001 (2006).
29. Lees, J. P. et al. Measurement of angular asymmetries in the decays $B \to K^*\ell^+\ell^-$. *Phys. Rev. D* **93**, 052015 (2016).
30. Wei J.-T. et al. Measurement of the differential branching fraction and forward-backward asymmetry for $B \to K^{(*)}\ell^+\ell^-$. *Phys. Rev. Lett.* **103**, 171801 (2009).
31. Wehle, S. et al. Lepton-flavor-dependent angular analysis of $B \to K^*\ell^+\ell^-$. *Phys. Rev. Lett.* **118**, 111801 (2017).
32. Aaltonen, T. et al. Measurements of the angular distributions in the decays $B \to K^{(*)}\mu^+\mu^-$ at CDF. *Phys. Rev. Lett.* **108**, 081807 (2012).
33. CMS collaboration Angular analysis of the decay $B^0 \to K^{*0}\mu^+\mu^-$ from pp collisions at $\sqrt{s} = 8$ TeV. *Phys. Lett. B* **753**, 424–448 (2016).
34. The CMS collaboration Measurement of angular parameters from the decay $B^0 \to K^{*0}\mu^+\mu^-$ in proton-proton collisions at $\sqrt{s} = 8$ TeV. *Phys. Lett.* B **781**, 517–541 (2018).
35. The LHCb collaboration et al. Measurements of the S-wave fraction in $B^0 \to K^+\pi^-\mu^+\mu^-$ decays and the $B^0 \to K^*(892)^0\mu^+\mu^-$ differential branching fraction. *J. High Energy Phys.* **2016**, 47 (2016); erratum **2017**, 142 (2017).
36. The LHCb collaboration et al. Angular analysis and differential branching fraction of the decay $B_s^0 \to \phi\mu^+\mu^-$. *J. High Energy Phys.* 2015, 179 (2015).
37. The LHCb collaboration et al. Differential branching fractions and isospin asymmetries of $B \to K^{(*)}\mu^+\mu^-$ decays. *J. High Energy Phys.* **2014**, 133 (2014).
38. The LHCb collaboration et al. Differential branching fraction and angular analysis of $\Lambda_b^0 \to \Lambda\mu^+\mu^-$ decays. *J. High Energy Phys.* **2015**, 115 (2015); erratum **2018**, 145 (2018).
39. Lyon, J., & Zwicky, R. Resonances gone topsy turvy—the charm of QCD or new physics in $b \to s\ell^+\ell^-$? Preprint at https://arxiv.org/abs/1406.0566 (2014).
40. Khodjamirian, A., Mannel, T. & Wang, Y.-M. $B \to K\ell^+\ell^-$ decay at large hadronic recoil. *J. High. Energy Phys.* **2013**, 010 (2013).
41. Khodjamirian, A., Mannel, T., Pivovarov, A. A. & Wang, Y.-M. Charm-loop effect in $B \to K^{(*)}\ell^+\ell^-$ and $B \to K^*\gamma$. *J. High Energy Phys.* **2010**, 89 (2010).
42. Descotes-Genon, S., Hofer, L., Matias, J. & Virto, J. On the impact of power corrections in the prediction of $B \to K^*\mu^+\mu^-$ observables. *J. High. Energy Phys.* **2014**, 125 (2014).
43. Horgan, R. R., Liu, Z., Meinel, S. & Wingate, M. Calculation of $B^0 \to K^{*0}\mu^+\mu^-$ and $B_s^0 \to \phi\mu^+\mu^-$ observables using form factors from lattice QCD. *Phys. Rev. Lett.* **112**, 212003 (2014).
44. Beaujean, F., Bobeth, C. & van Dyk, D. Comprehensive Bayesian analysis of rare (semi)leptonic and radiative B decays. *Eur. Phys. J. C* **74**, 2897 (2014); erratum **74**, 3179 (2014).
45. Hambrock, C., Hiller, G., Schacht, S. & Zwicky, R. $B \to K^*$ form factors from flavor data to QCD and back. *Phys. Rev. D* **89**, 074014 (2014).
46. Altmannshofer, W. & Straub, D. M. New physics in $B \to K^*\mu\mu$? *Eur. Phys. J. C* **73**, 2646 (2013).
47. Bobeth, C., Chrzaszcz, M., van Dyk, D. & Virto, J. Long-distance effects in $B \to K^*\ell\ell$ from analyticity. *Eur. Phys. J. C* **78**, 451 (2018).
48. Ciuchini, M. et al. Lessons from the $B^{0,+} \to K^{*0,+}\mu^+\mu^-$ angular analyses. *Phys. Rev. D* **103**, 015030 (2021).
49. Kowalska, K., Kumar, D. & Sessolo, E. M. Implications for new physics in $b \to s\mu\mu$ transitions after recent measurements by Belle and LHCb. *Eur. Phys. J. C* **79**, 840 (2019).
50. Alguerő, M. et al. Emerging patterns of new physics with and without lepton flavour universal contributions. *Eur. Phys. J. C* **79**, 714 (2019); addendum **80**, 511 (2020).

51. Hurth, T., Mahmoudi, F. & Neshatpour, S. Implications of the new LHCb angular analysis of $B \to K^* \mu^+ \mu^-$: hadronic effects or new physics? *Phys. Rev. D* **102**, 055001 (2020).
52. Ciuchini, M. et al. New physics in $b \to s\ell^+\ell^-$ confronts new data on lepton universality. *Eur. Phys. J. C* **79**, 719 (2019).
53. Aebischer, J. et al. *B*-decay discrepancies after Moriond 2019. *Eur. Phys. J. C* **80**, 252 (2020).
54. Alok, A. K., Dighe, A., Gangal, S. & Kumar, D. Continuing search for new physics in $b \to s\mu\mu$ decays: two operators at a time. *J. High. Energy Phys.* **2019**, 89 (2019).
55. Lees, J. P. et al. Evidence for an excess of $\overline{B} \to D^{(*)}\tau^-\overline{\nu}_\tau$ decays. *Phys. Rev. Lett.* **109**, 101802 (2012).
56. Aaij, R. et al. Measurement of the ratio of branching fractions $\mathcal{B}(B_c^+ \to J/\psi\tau^+\nu_\tau)/\mathcal{B}\mathcal{B}(B_c^+ \to J/\psi\mu^+\nu_\mu)$. *Phys. Rev. Lett.* **120**, 121801 (2018).
57. Lees, J. P. et al. Measurement of an excess of $\overline{B} \to D^{(*)}\tau^-\overline{\nu}_\tau$ decays and implications for charged Higgs bosons. *Phys. Rev. D* **88**, 072012 (2013).
58. Sato, Y. et al. Measurement of the branching ratio of $\overline{B}^0 \to D^{*+}\tau^-\overline{\nu}_\tau$ relative to $\overline{B}^0 \to D^{*+}\ell^-\overline{\nu}_\ell$ decays with a semileptonic tagging method. *Phys. Rev. D* **94**, 072007 (2016).
59. Aaij, R. et al. Measurement of the ratio of branching fractions $\mathcal{B}(\overline{B}^0 \to D^{*+}\tau^-\overline{\nu}_\tau)/\mathcal{B}(\overline{B}^0 \to D^{*+}\mu^-\overline{\nu}_\mu)$. *Phys. Rev. Lett.* **115**, 111803 (2015); erratum **115**, 159901 (2015).
60. Huschle, M. et al. Measurement of the branching ratio of $B^0 \to D^{(*)}\tau^-\overline{\nu}_\tau$ relative to $\overline{B} \to D^{(*)}\ell^-\overline{\nu}_\ell$ decays with hadronic tagging at Belle. *Phys. Rev. D* **92**, 072014 (2015).
61. Aaij, R. et al. Test of lepton flavor universality by the measurement of the $B^0 \to D^{*-}\tau^+\nu_\tau$ branching fraction using three-prong τ decays. *Phys. Rev. D* **97**, 072013 (2018).
62. Caria, G. et al. Measurement of $\mathcal{R}(D)$ and $\mathcal{R}(D^*)$ with a semileptonic tagging method. *Phys. Rev. Lett.* **124**, 161803 (2020).
63. Hirose, S. et al. Measurement of the τ lepton polarization and $R(D^*)$ in the decay $\overline{B} \to D^*\tau^-\overline{\nu}_\tau$ with one-prong hadronic τ decays at Belle. *Phys. Rev. D* **97**, 012004 (2018).
64. Aaij, R. et al. Test of lepton universality using $B^+ \to K^+\ell^+\ell^-$ decays. *Phys. Rev. Lett.* **113**, 151601 (2014).
65. Ablikim, M. et al. Precision measurements of $\mathcal{B}[\psi(3686) \to \pi^+\pi^- J/\psi]$ and $\mathcal{B}[J/\psi \to \ell^+\ell^-]$. *Phys. Rev. D* **88**, 032007 (2013).
66. Khodjamirian, A. & Rusov, A. V. $B_s \to K\ell\nu_\ell$ and $B_{(s)} \to \pi(K)\ell^+\ell^-$ decays at large recoil and CKM matrix elements. *J. High. Energy Phys.* **2017**, 112 (2017).
67. Altmannshofer, W. & Yavin, I. Predictions for lepton flavor universality violation in rare *B* decays in models with gauged $L_\mu - L_\tau$. *Phys. Rev. D* **92**, 075022 (2015).
68. Geng, L.-S. et al. Towards the discovery of new physics with lepton-universality ratios of $b \to s\ell\ell$ decays. *Phys. Rev. D* **96**, 093006 (2017).
69. Aaij, R. et al. Search for the decays $B_s^0 \to \tau^+\tau^-$ and $B^0 \to \tau^+\tau^-$. *Phys. Rev. Lett.* **118**, 251802 (2017).
70. Lees, J. P. et al. Search for $B^+ \to K^+\tau^+\tau^-$ at the BaBar experiment. *Phys. Rev. Lett.* **118**, 031802 (2017).
71. LHCb collaboration Physics case for an LHCb upgrade II—opportunities in flavour physics, and beyond, in the HL-LHC era. *CERN* https://cds.cern.ch/record/2636441 (2019).
72. Kou, E. et al. The Belle II physics book. *Prog. Theor. Exp. Phys.* **2019**, 123C01 (2019); erratum **2020**, 029201 (2020).
73. Bainbridge, R. on behalf of the CMS collaboration Recording and reconstructing 10 billion unbiased b hadron decays in CMS. *EPJ Web Conf.* **24**, 01025 (2020).
74. Aad, G. et al. Performance of the ATLAS level-1 topological trigger in run 2. *Eur. Phys. J. C* **82**, 7 (2022).

Methods

Experimental setup. The Large Hadron Collider (LHC) is the world's highest-energy particle accelerator and is situated approximately 100 m underground, close to Geneva, Switzerland. The collider accelerates two counter-rotating beams of protons, guided by superconducting magnets located around a 27 km circular tunnel, and brings them into collision at four interaction points that house large detectors. The LHCb experiment[75,76] is instrumented in the region covering the polar angles between 10 and 250 mrad around the proton beam axis, in which the products from B hadron decays can be efficiently captured and identified. The detector includes a high-precision tracking system with a dipole magnet, providing measurements of momentum and impact parameter (IP), defined for charged particles as the minimum distance of a track to a primary proton–proton interaction vertex (PV). Different types of charged particles are distinguished using information from two ring-imaging Cherenkov detectors, a calorimeter and a muon system[76].

Since the associated data storage and analysis costs would be prohibitive, the experiment does not record all collisions. Only potentially interesting events, selected using real-time event filters referred to as triggers, are recorded. The LHCb trigger system has a hardware stage, based on information from the calorimeter and muon systems, followed by a software stage that uses all the information from the detector, including the tracking, to make the final selection of events to be recorded for subsequent analysis. The trigger selection algorithms are based on identifying key characteristics of B hadrons and their decay products, such as high p_T final-state particles, and a decay vertex that is significantly displaced from any of the PVs in the event.

For the R_K measurement, candidate events are required to have passed a hardware trigger algorithm that selects either a high-p_T muon, or an electron, hadron or photon with high transverse energy deposited in the calorimeters. The $B^+ \to K^+\mu^+\mu^-$ and $B^+ \to J/\psi(\to \mu^+\mu^-)K^+$ candidates must be triggered by one of the muons, whereas $B^+ \to K^+e^+e^-$ and $B^+ \to J/\psi(\to e^+e^-)K^+$ candidates must be triggered in one of three ways: by either one of the electrons, by the kaon from the B^+ decay or by other particles in the event that are not decay products of the B^+ candidate. In the software trigger, the tracks of the final-state particles are required to form a displaced vertex with good fit quality. A multivariate algorithm is used for the identification of displaced vertices consistent with the decay of a B hadron[77,78].

Analysis description. The analysis technique used to obtain the results presented in this paper is essentially identical to that used to obtain the previous LHCb R_K measurement, described in ref. [11], and only the main analysis steps are reviewed here.

Event selection. Kaon and muon candidates are identified using the output of multivariate classifiers that exploit information from the tracking system, the ring-imaging Cherenkov detectors, the calorimeters and the muon chambers. Electrons are identified by matching tracks to particle showers in the electromagnetic calorimeter (ECAL) and using the ratio of the energy detected in the ECAL to the momentum measured by the tracking system. An electron that emits a bremsstrahlung photon due to interactions with the material of the detector downstream of the dipole magnet results in the photon and electron depositing their energy in the same ECAL cells and therefore in a correct measurement of the original energy of the electron in the ECAL. However, a bremsstrahlung photon emitted upstream of the magnet will deposit energy in a different part of the ECAL than the electron, which is deflected in the magnetic field. For each electron track, a search is therefore made in the ECAL for energy deposits around the extrapolated track direction before the magnet that are not associated with any other charged tracks. The energy of any such deposit is added to the electron energy that is derived from the measurements made in the tracker. Bremsstrahlung photons can be added to none, either or both of the final-state e^+ and e^- candidates.

To suppress background, each final-state particle is required to have sizeable p_T and to be inconsistent with coming from a PV. The particles are required to originate from a common vertex, with good vertex-fit quality, that is displaced significantly from all of the PVs in the event. The PVs are reconstructed by searching for space points where an accumulation of track trajectories is observed. A weighted least-squares method is then employed to find the precise vertex position. The B^+ momentum vector is required to be aligned with the vector connecting one of the PVs in the event (below referred to as the associated PV) and the B^+ decay vertex. The value of q^2 is calculated using only the lepton momenta, without imposing any constraint on the $m(K^+\ell^+\ell^-)$ mass.

The $m(K^+\ell^+\ell^-)$ mass ranges and the q^2 regions used to select the different decay modes are shown in Extended Data Table 1. The selection requirements applied to the non-resonant and resonant decays are otherwise identical. For the muon modes, the superior mass resolution allows a fit in a reduced $m(K^+\ell^+\ell^-)$ mass range compared with the electron modes. For the electron modes, a wider mass region is needed to perform an accurate fit, but the range chosen suppresses any significant contribution from decays with two or more additional pions that are not reconstructed. The residual contribution from such decays is considered as a source of systematic uncertainty. Resolution effects similarly motivate the choice of non-resonant q^2 regions, with a lower limit that excludes contributions from ϕ-meson decays and an upper limit that reduces the tail from $B^+ \to J/\psi(\to e^+e^-)K^+$ decays. The proportion of signal candidates that migrate in and out of the q^2 region of interest is on the order of 10%. This effect is accounted for using simulation (Extended Data Figs. 7 and 8).

Cascade background of the form $B \to H_c(\to K^+\ell^-\overline{\nu}_\ell X)\ell^+\nu_\ell Y$, where H_c is a hadron containing a c quark (D^0, D^+, D_s^+, Λ_c^+), and X, Y are particles that are not included in the B^+ candidate, are suppressed by requiring that the kaon–lepton invariant mass is in the region $m(K^+\ell^-) > m_{D^0}$, where m_{D^0} is the known D^0 mass[2]. For the electron mode, this requirement is illustrated in Extended Data Fig. 1 (left). Analogous background sources with a misidentified particle are reduced by applying a similar veto, but with the lepton mass hypothesis changed to that of a pion (denoted $\ell_{[\to\pi]}$). In the muon case, $K\mu_{[\to\pi]}$ combinations with mass smaller than m_{D^0} are rejected. In the electron case, a ± 40 MeV c^{-2} window around the D^0 mass is used to reject candidates where the veto is applied without the bremsstrahlung recovery, that is, on the basis of only the measured track momenta. The mass distributions are shown in Extended Data Fig. 1. The electron and muon veto cuts differ given the relative helicity suppression of $\pi^+ \to \ell^+\nu_\ell$ decays. This causes misidentification backgrounds to populate a range of $K\mu$ masses but only a peak in the Ke mass. The veto requirements retain 97% of $B^+ \to K^+\mu^+\mu^-$ and 95% of $B^+ \to K^+e^+e^-$ decays passing all other selection requirements.

Background from other exclusive B-hadron decays requires at least two particles to be misidentified. These include the decays $B^+ \to K^+\pi^+\pi^-$, and misreconstructed $B^+ \to J/\psi(\to \ell^+\ell^-)K^+$ and $B^+ \to \psi(2S)(\to \ell^+\ell^-)K^+$ decays. In the latter two decays, the kaon is misidentified as a lepton and the lepton (of the same electric charge) as a kaon. Such background is reduced to a negligible level by particle identification criteria. Background from decays with a photon converted into an e^+e^- pair are also negligible due to the q^2 selection.

Multivariate selection. A boosted decision tree (BDT) algorithm[79] with gradient boosting[80] is used to reduce combinatorial background. For the non-resonant muon mode and for each of the three different trigger categories of the non-resonant electron mode, a single BDT classifier is trained for the 7 and 8 TeV data, and an additional classifier is trained for the 13 TeV data. The BDT output is not strongly correlated with q^2, and the same classifiers are used to select the respective resonant decays. To train the classifier, simulated non-resonant $B^+ \to K^+\ell^+\ell^-$ decays are used as a proxy for the signal and non-resonant $K^+\ell^+\ell^-$ candidates selected from the data with $m(K^+\ell^+\ell^-) > 5.4\,\text{GeV}\,c^{-2}$ are used as a background sample. The k-folding technique is used in the training and testing[81]. The classifier includes the following variables: the p_T of the B^+, K^+ and dilepton candidates, and the minimum and maximum p_T of the leptons; the B^+, dilepton and K^+ χ^2_{IP} with respect to the associated PV, where χ^2_{IP} is defined as the difference in the vertex-fit χ^2 of the PV reconstructed with and without the considered particle; the minimum and maximum χ^2_{IP} of the leptons; the B^+ vertex-fit quality; the statistical significance of the B^+ flight distance; and the angle between the B^+ candidate momentum vector and the direction between the associated PV and the B^+ decay vertex. The p_T of the final state particles, the vertex-fit χ^2 and the significance of the flight distance have the most discriminating power. For each of the classifiers, a requirement is placed on the output variable to maximize the predicted significance of the non-resonant signal yield. For the electron modes that dictate the R_K precision, this requirement reduces the combinatorial background by approximately 99% while retaining 85% of the signal mode. The muon BDT classifier has similar performance. In both cases, for both signal and background, the efficiency of the BDT selection has negligible dependence on $m(K^+\ell^+\ell^-)$ and q^2 in the regions used to determine the event yields.

Calibration of simulation. The simulated data used in this analysis are produced using the software described in refs. [82–88]. Bremsstrahlung emission in the decay of particles is simulated using the PHOTOS software in the default configuration[89], which is observed to agree with an independent quantum electrodynamics calculation at the level of 1% (ref. [5]).

Simulated events are weighted to correct for the imperfect modelling using control channels. The B^+ production kinematics are corrected using $B^+ \to J/\psi(\to \ell^+\ell^-)K^+$ events. The particle identification performance is calibrated using data, where the species of particles in the final state can be unambiguously determined purely on the basis of the kinematics. The calibration samples consist of $D^{*+} \to D^0(\to K^-\pi^+)\pi^+$, $J/\psi \to \mu^+\mu^-$ and $B^+ \to J/\psi(\to e^+e^-)K^+$ decays, from which kaons, muons and electrons, respectively, can be selected without applying particle identification requirements. The performance of the particle identification requirements is then evaluated from the proportion of events in these samples which fulfil the particle identification selection criteria. The trigger response is corrected using weights applied to simulation as a function of variables relevant to the trigger algorithms. The weights are calculated by requiring that simulated $B^+ \to J/\psi(\to \ell^+\ell^-)K^+$ events exhibit the same trigger performance as the control data. The $B^+ \to J/\psi(\to \ell^+\ell^-)K^+$ events selected from the data have also been used to demonstrate control of the electron track reconstruction efficiency at the percent level[90]. Whenever $B^+ \to J/\psi(\to \ell^+\ell^-)K^+$ events are used to correct the simulation, the correlations between calibration and measurement samples are taken into account in the results and cross-checks presented in this paper. The correlation is evaluated using a bootstrapping method to recompute the yields and efficiencies many times with different subsets of the data.

Likelihood fit. An unbinned extended maximum-likelihood fit is made to the $m(K^+e^+e^-)$ and $m(K^+\mu^+\mu^-)$ distributions of non-resonant candidates. The value of R_K is a fit parameter, which is related to the signal yields and efficiencies according to

$$R_K = \frac{N(B^+\to K^+\mu^+\mu^-)}{\varepsilon(B^+\to K^+\mu^+\mu^-)}\cdot\frac{\varepsilon(B^+\to K^+e^+e^-)}{N(B^+\to K^+e^+e^-)} \times\frac{\varepsilon(B^+\to J/\psi(\to\mu^+\mu^-)K^+)}{N(B^+\to J/\psi(\to\mu^+\mu^-)K^+)}\cdot\frac{N(B^+\to J/\psi(\to e^+e^-)K^+)}{\varepsilon(B^+\to J/\psi(\to e^+e^-)K^+)}, \quad (4)$$

where $N(X)$ indicates the yield of decay mode X and $\varepsilon(X)$ is the efficiency for selecting decay mode X. The resonant yields are determined from separate fits to $m_{J/\psi}(K^+\ell^+\ell^-)$. In the fit for R_K, these yields and the efficiencies are incorporated as Gaussian-constraint terms.

To take into account the correlation between the selection efficiencies, the $m(K^+e^+e^-)$ and $m(K^+\mu^+\mu^-)$ distributions of non-resonant candidates in each of the different trigger categories and data-taking periods are fitted simultaneously, with a common value of R_K. The relative fraction of partially reconstructed background in each trigger category is also shared across the different data-taking periods.

The mass-shape parameters are derived from the calibrated simulation. The four signal modes are modelled by multiple Gaussian functions with power-law tails on both sides of the peak[91,92], although the differing detector response gives different shapes for the electron and muon modes. The signal mass shapes of the electron modes are described with the sum of three distributions, which model whether the ECAL energy deposit from a bremsstrahlung photon was added to both, either or neither of the $e^\pm$ candidates. The expected values from simulated events are used to constrain the fraction of signal decays in each of these categories. These fractions are observed to agree well with those observed in resonant events selected from the data. To take into account residual differences in the signal shape between data and simulation, an offset in the peak position and a scaling of the resolution are allowed to vary in the fits to the resonant modes. The corresponding parameters are then fixed in the fits to the relevant non-resonant modes. This resolution scaling changes the migration of candidates into the q^2 region of interest by less than 1%.

For the modelling of non-resonant and resonant partially reconstructed backgrounds, data are used to correct the simulated $K\pi$ mass spectrum for $B^{(0,+)}\to K^+\pi^{(-,0)}e^+e^-$ and $B^{(0,+)}\to J/\psi(\to e^+e^-)K^+\pi^{(-,0)}$ decays[93]. The calibrated simulation is used subsequently to obtain the $m(K^+\ell^+\ell^-)$ mass shape and relative fractions of these background components. To accommodate possible lepton universality violation in these partially reconstructed processes, which are underpinned by the same $\bar{b}\to\bar{s}$ quark-level transitions as those of interest, the overall yield of such decays is left to vary freely in the fit. The shape of the $B^+\to J/\psi\pi^+$ background contribution is taken from simulation, but the size with respect to the $B^+\to J/\psi K^+$ mode is constrained using the known ratio of the relevant branching fractions[2,94] and efficiencies.

In the fits to non-resonant $B^+\to K^+e^+e^-$ candidates, the mass shape of the background from $B^+\to J/\psi(\to e^+e^-)K^+$ decays with an emitted photon that is not reconstructed is also taken from simulation and, adjusting for the relevant selection efficiency, its yield is constrained to the value from the fit to the resonant mode within its uncertainty. In all fits, the combinatorial background is modelled with an exponential function with a freely varying yield and shape.

The fits to the non-resonant (resonant) decay modes in different data-taking periods and trigger categories are shown in Extended Data Fig. 2 (Extended Data Fig. 3). For the resonant modes, the results from independent fits to each period/category are shown. Conversely, the non-resonant distributions show the projections from the simultaneous fit across data-taking periods and trigger categories that is used to obtain R_K. The fitted yields for the resonant and non-resonant decays are given in Extended Data Table 2.

The profile likelihood for the fit to the non-resonant decays is shown in Extended Data Fig. 4. The likelihood is non-Gaussian in the region $R_K > 0.95$ due to the comparatively low yield of $B^+\to K^+e^+e^-$ events. Following the procedure described in refs. [11,12], the P value is computed by integrating the posterior probability density function for R_K, having folded in the theory uncertainty on the SM prediction, for R_K values larger than the SM expectation. The corresponding significance in terms of standard deviations is computed using the inverse Gaussian cumulative distribution function for a one-sided conversion.

A test statistic is constructed that is based on the likelihood ratio between two hypotheses with common (null) or different (test) R_K values for the part of the sample analysed previously (7, 8 and part of the 13 TeV data) and for the new portion of the 13 TeV data. Using pseudo-experiments based on the null hypothesis, the data suggest that the R_K value from the new portion of the data is compatible with that from the previous sample with a P value of 95%. Further tests give good compatibility for subsamples of the data corresponding to different trigger categories and magnet polarities.

The departure of the profile likelihood shown in Extended Data Fig. 4 from a normal distribution stems from the definition of R_K. In particular, in the R_K ratio, the denominator is affected by larger statistical uncertainties than the numerator, owing to the larger number of non-resonant muonic signal candidates. However, the intervals of the likelihood distribution are found to be the same when estimated with $1/R_K$ as the fit parameter.

Additional cross-checks. The $r_{J/\psi}$ single ratio is used to perform a number of additional cross-checks. The distribution of this ratio as a function of the angle between the leptons and the minimum p_T of the leptons is shown in Extended Data Fig. 5, together with the spectra expected for the resonant and non-resonant decays. No significant trend is observed in either $r_{J/\psi}$ distribution. Assuming that the deviations observed are genuine mis-modelling of the efficiencies, rather than statistical fluctuations, a total shift of R_K at a level less than 0.001 would be expected due to these effects. This estimate takes into account the spectrum of the relevant variables in the non-resonant decay modes of interest and is compatible with the estimated systematic uncertainties on R_K. Similarly, the variations seen in $r_{J/\psi}$ as a function of all other reconstructed quantities examined are compatible with the systematic uncertainties assigned. In addition, $r_{J/\psi}$ is computed in two-dimensional intervals of reconstructed quantities (Extended Data Fig. 6). Again, no significant trend is seen.

Systematic uncertainties. The majority of the sources of systematic uncertainty affect the relative efficiencies between non-resonant and resonant decays. These are included in the fit to R_K by allowing the relative efficiency to vary within Gaussian constraints. The width of the constraint is determined by adding the contributions from the different sources in quadrature. Correlations in the systematic uncertainties between different trigger categories and run periods are taken into account. Systematic uncertainties affecting the determination of the signal yield are assessed using pseudo-experiments generated with variations of the fit model. Pseudo-experiments are also used to assess the degree of bias originating from the fitting procedure. The bias is found to be 1% of the statistical precision and thus negligible with respect to other sources of systematic uncertainty.

For the non-resonant $B^+\to K^+e^+e^-$ decays, the systematic uncertainties are dominated by the modelling of the signal and background components used in the fit. The effect on R_K is at the 1% level. A significant proportion (0.7%) of this uncertainty comes from the limited knowledge of the $K\pi$ spectrum in $B^{(0,+)}\to K^+\pi^{(-,0)}e^+e^-$ decays. In addition, a 0.2% systematic uncertainty is assigned for the potential contribution from partially reconstructed decays with two additional pions. An uncertainty comparable to that from the modelling of the signal and background components is induced by the limited sizes of calibration samples. Other sources of systematic uncertainty, such as the calibration of B^+ production kinematics, the trigger calibration and the determination of the particle identification efficiencies, contribute at the few-permille or permille level, depending strongly on the data-taking period and the trigger category.

The uncertainties on parameters used in the simulation model of the signal decays affect the q^2 distribution and hence the selection efficiency. These uncertainties are propagated to an uncertainty on R_K using predictions from the FLAVIO software package[7] but give rise to a negligible effect. Similarly, the differing q^2 resolution between data and simulation, which alters estimates of the q^2 migration, has negligible impact on the result.

Data availability

LHCb data used in this analysis will be released according to the LHCb external data access policy, which can be downloaded from http://opendata.cern.ch/record/410/files/LHCb-Data-Policy.pdf. The raw data in all of the figures of this paper, and additional supplementary material, can be downloaded from https://cds.cern.ch/record/2758740, where no access codes are required. In addition, the likelihood profile shown in Extended Data Fig. 4 has been added to the HEPData platform at https://www.hepdata.net/record/ins1852846?version=1.

Code availability

LHCb software used to process the data analysed in this paper is available at https://gitlab.cern.ch/lhcb.

References

75. LHCb collaboration et al. The LHCb detector at the LHC. *J. Instrum.* **3**, S08005 (2008).
76. LHCb collaboration LHCb detector performance. *Int. J. Mod. Phys. A* **30**, 1530022 (2015).
77. Gligorov, V. V. & Williams, M. Efficient, reliable and fast high-level triggering using a bonsai boosted decision tree. *J. Instrum.* **8**, P02013 (2013).
78. Likhomanenko, T. et al. LHCb topological trigger reoptimization. *J. Phys. Conf. Ser.* **664**, 082025 (2015).
79. Breiman, L., Friedman, J. H., Olshen, R. A., & Stone C. J. *Classification and Regression Trees* (Wadsworth, 1984).
80. Huber, P. J. in *Robust Estimation of a Location Parameter* (eds Kotz S. & Johnson N. L.) 492–518 (Springer, 1992).
81. Blum, A., Kalai, A. & Langford J. Beating the hold-out: bounds for K-fold and progressive cross-validation. In *Proc. 12th Annual Conference on Computational Learning Theory, COLT '99* 203–208 (ACM, 1999).
82. Sjöstrand, T., Mrenna, S. & Skands, P. PYTHIA 6.4 physics and manual. *J. High Energy Phys.* **2006**, 026 (2006).
83. Sjöstrand, T., Mrenna, S. & Skands, P. A brief introduction to PYTHIA 8.1. *Comput. Phys. Commun.* **178**, 852–867 (2008).

84. Belyaev, I. et al. Handling of the generation of primary events in Gauss, the LHCb simulation framework. *J. Phys. Conf. Ser.* **331**, 032047 (2011).
85. Lange, D. J. The EvtGen particle decay simulation package. *Nucl. Instrum. Methods A* **462**, 152–155 (2001).
86. Allison, J. et al. Geant4 developments and applications, *IEEE Trans. Nucl. Sci.* **53**, 270–278 (2006).
87. Agostinelli, S. et al. Geant4: a simulation toolkit. *Nucl. Instrum. Methods A* **506**, 250–303 (2003).
88. Clemencic, M. et al. The LHCb simulation application, Gauss: design, evolution and experience. *J. Phys. Conf. Ser.* **331**, 032023 (2011).
89. Davidson, N., Przedzinski, T. & Was, Z. PHOTOS interface in C++: technical and physics documentation. *Comput. Phys. Commun.* **199**, 86–101 (2016).
90. Aaij, R. et al. Measurement of the electron reconstruction efficiency at LHCb. *J. Instrum.* **14**, P11023 (2019).
91. Skwarnicki, T. *A Study of the Radiative Cascade Transitions between the Upsilon-Prime and Upsilon Resonances*. PhD thesis, Institute of Nuclear Physics, Krakow (1986).
92. Martínez Santos, D. & Dupertuis, F. Mass distributions marginalized over per-event errors. *Nucl. Instrum. Methods A* **764**, 150–155 (2014).
93. LHCb collaboration et al. Differential branching fraction and angular analysis of the decay $B^0 \to K^+ l - \mu + \mu -$ in the $K^*_{0,2}(1430)^0$ region. *J. High Energy Phys.* **2016**, 65 (2016).
94. LHCb collaboration et al. Measurement of the ratio of branching fractions and difference in *CP* asymmetries of the decays $B^+ \to J/\psi\pi^+$ and $B^+ \to J/\psi K^+$. *J. High Energy Phys.* **2017**, 36 (2017).

Acknowledgements

We thank our colleagues in the CERN accelerator departments for the excellent performance of the LHC, and the technical and administrative staff at the LHCb institutes. We acknowledge support from CERN and from the national agencies: CAPES, CNPq, FAPERJ and FINEP (Brazil); MOST and NSFC (China); CNRS/IN2P3 (France); BMBF, DFG and MPG (Germany); INFN (Italy); NWO (Netherlands); MNiSW and NCN (Poland); MEN/IFA (Romania); MSHE (Russia); MICINN (Spain); SNSF and SER (Switzerland); NASU (Ukraine); STFC (United Kingdom); DOE NP and NSF (United States). We acknowledge the computing resources that are provided by CERN, IN2P3 (France), KIT and DESY (Germany), INFN (Italy), SURF (the Netherlands), PIC (Spain), GridPP (United Kingdom), RRCKI and Yandex LLC (Russia), CSCS (Switzerland), IFIN-HH (Romania), CBPF (Brazil), PL-GRID (Poland) and NERSC (United States). We are indebted to the communities behind the multiple open-source software packages on which we depend. Individual groups or members have received support from ARC and ARDC (Australia); AvH Foundation (Germany); EPLANET, Marie Skłodowska-Curie Actions and ERC (European Union); A*MIDEX, ANR, Labex P2IO and OCEVU, and Région Auvergne-Rhône-Alpes (France); Key Research Program of Frontier Sciences of CAS, CAS PIFI, CAS CCEPP, Fundamental Research Funds for the Central Universities, and Sci. & Tech. Program of Guangzhou (China); RFBR, RSF and Yandex LLC (Russia); GVA, XuntaGal and GENCAT (Spain); the Leverhulme Trust, the Royal Society and UKRI (United Kingdom).

Author contributions

All contributing authors, as listed at the end of the manuscript, have contributed to the publication, being variously involved in the design and construction of the detector, writing software, calibrating sub-systems, operating the detector, acquiring data and analysing the processed data.

Competing interests

The authors declare no competing interests.

Additional information

Extended data is available for this paper at https://doi.org/10.1038/s41567-021-01478-8.

Supplementary information The online version contains supplementary material available at https://doi.org/10.1038/s41567-021-01478-8.

Correspondence and requests for materials should be addressed to A. Bertolin.

Peer review information *Nature Physics* thanks Akimasa Ishikawa, Marcella Bona and the other, anonymous, reviewer(s) for their contribution to the peer review of this work.

LHCb collaboration

R. Aaij[1], C. Abellán Beteta[2], T. Ackernley[3], B. Adeva[4], M. Adinolfi[5], H. Afsharnia[6], C. A. Aidala[7], S. Aiola[8], Z. Ajaltouni[6], S. Akar[9], J. Albrecht[10], F. Alessio[11], M. Alexander[12], A. Alfonso Albero[13], Z. Aliouche[14], G. Alkhazov[15], P. Alvarez Cartelle[16], S. Amato[17], Y. Amhis[18], L. An[11], L. Anderlini[19], A. Andreianov[15], M. Andreotti[20], F. Archilli[21], A. Artamonov[22], M. Artuso[23], K. Arzymatov[24], E. Aslanides[25], M. Atzeni[2], B. Audurier[26], S. Bachmann[21], M. Bachmayer[27], J. J. Back[28], P. Baladron Rodriguez[4], V. Balagura[26], W. Baldini[20], J. Baptista Leite[29], R. J. Barlow[14], S. Barsuk[18], W. Barter[30], M. Bartolini[31], F. Baryshnikov[32], J. M. Basels[33], G. Bassi[34], B. Batsukh[23], A. Battig[10], A. Bay[27], M. Becker[10], F. Bedeschi[34], I. Bediaga[29], A. Beiter[23], V. Belavin[24], S. Belin[35], V. Bellee[27], K. Belous[22], I. Belov[36], I. Belyaev[37], G. Bencivenni[38], E. Ben-Haim[39], A. Berezhnoy[36], R. Bernet[2], D. Berninghoff[21], H. C. Bernstein[23], C. Bertella[11], A. Bertolin[40] ✉, C. Betancourt[2], F. Betti[11], Ia. Bezshyiko[2], S. Bhasin[5], J. Bhom[41], L. Bian[42], M. S. Bieker[10], S. Bifani[43], P. Billoir[39], M. Birch[30], F. C. R. Bishop[16], A. Bitadze[14], A. Bizzeti[19,44], M. Bjørn[45], M. P. Blago[11], T. Blake[28], F. Blanc[27], S. Blusk[23], D. Bobulska[12], J. A. Boelhauve[10], O. Boente Garcia[4], T. Boettcher[46], A. Boldyrev[47], A. Bondar[48], N. Bondar[11,15], S. Borghi[14], M. Borisyak[24], M. Borsato[21], J. T. Borsuk[41], S. A. Bouchiba[27], T. J. V. Bowcock[3], A. Boyer[11], C. Bozzi[20], M. J. Bradley[30], S. Braun[49], A. Brea Rodriguez[4], M. Brodski[11], J. Brodzicka[41], A. Brossa Gonzalo[28], D. Brundu[35], A. Buonaura[2], C. Burr[11], A. Bursche[50], A. Butkevich[51], J. S. Butter[1], J. Buytaert[11], W. Byczynski[11], S. Cadeddu[35], H. Cai[42], R. Calabrese[20,52], L. Calefice[10,39], L. Calero Diaz[38], S. Cali[38], R. Calladine[43], M. Calvi[53,54], M. Calvo Gomez[55], P. Camargo Magalhaes[5], A. Camboni[13,55], P. Campana[38], A. F. Campoverde Quezada[56], S. Capelli[53,54], L. Capriotti[57,58], A. Carbone[57,58], G. Carboni[59], R. Cardinale[31], A. Cardini[35], I. Carli[60], P. Carniti[53,54], L. Carus[33], K. Carvalho Akiba[1], A. Casais Vidal[4], G. Casse[3], M. Cattaneo[11], G. Cavallero[11], S. Celani[27], J. Cerasoli[25], A. J. Chadwick[3], M. G. Chapman[5], M. Charles[39], Ph. Charpentier[11], G. Chatzikonstantinidis[43], C. A. Chavez Barajas[3], M. Chefdeville[61], C. Chen[62], S. Chen[60], A. Chernov[41], V. Chobanova[4], S. Cholak[27], M. Chrzaszcz[41], A. Chubykin[15], V. Chulikov[15], P. Ciambrone[38], M. F. Cicala[28], X. Cid Vidal[4], G. Ciezarek[11], P. E. L. Clarke[63], M. Clemencic[11], H. V. Cliff[16], J. Closier[11], J. L. Cobbledick[14], V. Coco[11], J. A. B. Coelho[18], J. Cogan[25], E. Cogneras[6], L. Cojocariu[64], P. Collins[11], T. Colombo[11], L. Congedo[65,66], A. Contu[35], N. Cooke[43], G. Coombs[12], G. Corti[11], C. M. Costa Sobral[28], B. Couturier[11], D. C. Craik[46], J. Crkovská[67], M. Cruz Torres[29], R. Currie[63], C. L. Da Silva[67], E. Dall'Occo[10], J. Dalseno[4], C. D'Ambrosio[11], A. Danilina[37], P. d'Argent[11], A. Davis[14], O. De Aguiar Francisco[14], K. De Bruyn[68], S. De Capua[14], M. De Cian[27], J. M. De Miranda[29], L. De Paula[17], M. De Serio[65,66], D. De Simone[2], P. De Simone[38], J. A. de Vries[69], C. T. Dean[67], D. Decamp[61], L. Del Buono[39], B. Delaney[16], H.-P. Dembinski[10], A. Dendek[70], V. Denysenko[2], D. Derkach[47], O. Deschamps[6], F. Desse[18], F. Dettori[35,71], B. Dey[72], P. Di Nezza[38], S. Didenko[32], L. Dieste Maronas[4], H. Dijkstra[11], V. Dobishuk[73], A. M. Donohoe[74], F. Dordei[35], A. C. dos Reis[29], L. Douglas[12], A. Dovbnya[75], A. G. Downes[61], K. Dreimanis[3], M. W. Dudek[41], L. Dufour[11], V. Duk[76], P. Durante[11], J. M. Durham[67], D. Dutta[14], A. Dziurda[41], A. Dzyuba[15], S. Easo[77], U. Egede[78], V. Egorychev[37], S. Eidelman[48,79], S. Eisenhardt[63], S. Ek-In[27], L. Eklund[12,80], S. Ely[23], A. Ene[64], E. Epple[67], S. Escher[33], J. Eschle[2], S. Esen[39], T. Evans[11], A. Falabella[57], J. Fan[62], Y. Fan[56], B. Fang[42], S. Farry[3], D. Fazzini[53,54], M. Féo[11], A. Fernandez Prieto[4], J. M. Fernandez-tenllado Arribas[13], A. D. Fernez[49], F. Ferrari[57,58], L. Ferreira Lopes[27], F. Ferreira Rodrigues[17], S. Ferreres Sole[1], M. Ferrillo[2], M. Ferro-Luzzi[11], S. Filippov[51], R. A. Fini[65], M. Fiorini[20,52], M. Firlej[70], K. M. Fischer[45], D. S. Fitzgerald[7], C. Fitzpatrick[14], T. Fiutowski[70], F. Fleuret[26], M. Fontana[39], F. Fontanelli[31,81], R. Forty[11], V. Franco Lima[3], M. Franco Sevilla[49], M. Frank[11],

E. Franzoso[20], G. Frau[21], C. Frei[11], D. A. Friday[12], J. Fu[8], Q. Fuehring[10], W. Funk[11], E. Gabriel[1], T. Gaintseva[24], A. Gallas Torreira[4], D. Galli[57,58], S. Gambetta[11,63], Y. Gan[62], M. Gandelman[17], P. Gandini[8], Y. Gao[82], M. Garau[35], L. M. Garcia Martin[28], P. Garcia Moreno[13], J. García Pardiñas[53,54], B. Garcia Plana[4], F. A. Garcia Rosales[26], L. Garrido[13], C. Gaspar[11], R. E. Geertsema[1], D. Gerick[21], L. L. Gerken[10], E. Gersabeck[14], M. Gersabeck[14], T. Gershon[28], D. Gerstel[25], Ph. Ghez[61], V. Gibson[16], H. K. Giemza[83], M. Giovannetti[38,84], A. Gioventù[4], P. Gironella Gironell[13], L. Giubega[64], C. Giugliano[11,20,71], K. Gizdov[63], E. L. Gkougkousis[11], V. V. Gligorov[39], C. Göbel[85], E. Golobardes[55], D. Golubkov[37], A. Golutvin[30,32], A. Gomes[29,86], S. Gomez Fernandez[13], F. Goncalves Abrantes[45], M. Goncerz[41], G. Gong[62], P. Gorbounov[37], I. V. Gorelov[36], C. Gotti[53], E. Govorkova[11], J. P. Grabowski[21], T. Grammatico[39], L. A. Granado Cardoso[11], E. Graugés[13], E. Graverini[27], G. Graziani[19], A. Grecu[64], L. M. Greeven[1], P. Griffith[20,52], L. Grillo[14], S. Gromov[32], B. R. Gruberg Cazon[45], C. Gu[62], M. Guarise[20], P. A. Günther[21], E. Gushchin[51], A. Guth[33], Y. Guz[22], T. Gys[11], T. Hadavizadeh[78], G. Haefeli[27], C. Haen[11], J. Haimberger[11], T. Halewood-leagas[3], P. M. Hamilton[49], J. P. Hammerich[3], Q. Han[87], X. Han[21], T. H. Hancock[45], S. Hansmann-Menzemer[21], N. Harnew[45], T. Harrison[3], C. Hasse[11], M. Hatch[11], J. He[56,88], M. Hecker[30], K. Heijhoff[1], K. Heinicke[10], A. M. Hennequin[11], K. Hennessy[3], L. Henry[8,89], J. Heuel[33], A. Hicheur[17], D. Hill[27], M. Hilton[14], S. E. Hollitt[10], J. Hu[21], J. Hu[50], W. Hu[87], W. Huang[56], X. Huang[42], W. Hulsbergen[1], R. J. Hunter[28], M. Hushchyn[47], D. Hutchcroft[3], D. Hynds[1], P. Ibis[10], M. Idzik[70], D. Ilin[15], P. Ilten[9], A. Inglessi[15], A. Ishteev[32], K. Ivshin[15], R. Jacobsson[11], S. Jakobsen[11], E. Jans[1], B. K. Jashal[89], A. Jawahery[49], V. Jevtic[10], M. Jezabek[41], F. Jiang[62], M. John[45], D. Johnson[11], C. R. Jones[16], T. P. Jones[28], B. Jost[11], N. Jurik[11], S. Kandybei[75], Y. Kang[62], M. Karacson[11], M. Karpov[47], F. Keizer[11], M. Kenzie[28], T. Ketel[90], B. Khanji[10], A. Kharisova[91], S. Kholodenko[22], T. Kirn[33], V. S. Kirsebom[27], O. Kitouni[46], S. Klaver[1], K. Klimaszewski[83], S. Koliiev[73], A. Kondybayeva[32], A. Konoplyannikov[37], P. Kopciewicz[70], R. Kopecna[21], P. Koppenburg[1], M. Korolev[36], I. Kostiuk[1,73], O. Kot[73], S. Kotriakhova[15,20], P. Kravchenko[15], L. Kravchuk[51], R. D. Krawczyk[11], M. Kreps[28], F. Kress[30], S. Kretzschmar[33], P. Krokovny[48,79], W. Krupa[70], W. Krzemien[83], W. Kucewicz[41,92], M. Kucharczyk[41], V. Kudryavtsev[48,79], H. S. Kuindersma[1,90], G. J. Kunde[67], T. Kvaratskheliya[37], D. Lacarrere[11], G. Lafferty[14], A. Lai[35], A. Lampis[35], D. Lancierini[2], J. J. Lane[14], R. Lane[5], G. Lanfranchi[38], C. Langenbruch[33], J. Langer[10], O. Lantwin[2], T. Latham[28], F. Lazzari[34,93], R. Le Gac[25], S. H. Lee[7], R. Lefèvre[6], A. Leflat[36], S. Legotin[32], O. Leroy[25], T. Lesiak[41], B. Leverington[21], H. Li[50], L. Li[45], P. Li[21], S. Li[87], Y. Li[60], Y. Li[60], Z. Li[23], X. Liang[23], T. Lin[30], R. Lindner[11], V. Lisovskyi[10], R. Litvinov[35], G. Liu[50], H. Liu[56], S. Liu[60], X. Liu[62], A. Loi[35], J. Lomba Castro[4], I. Longstaff[12], J. H. Lopes[17], G. H. Lovell[16], Y. Lu[60], D. Lucchesi[40,94], S. Luchuk[51], M. Lucio Martinez[1], V. Lukashenko[1], Y. Luo[62], A. Lupato[14], E. Luppi[20,52], O. Lupton[28], A. Lusiani[34,95], X. Lyu[56], L. Ma[60], R. Ma[56], S. Maccolini[57,58], F. Machefert[18], F. Maciuc[64], V. Macko[27], P. Mackowiak[10], S. Maddrell-Mander[5], O. Madejczyk[70], L. R. Madhan Mohan[5], O. Maev[15], A. Maevskiy[47], D. Maisuzenko[15], M. W. Majewski[70], J. J. Malczewski[41], S. Malde[45], B. Malecki[11], A. Malinin[96], T. Maltsev[48,79], H. Malygina[21], G. Manca[35,71], G. Mancinelli[25], D. Manuzzi[57,58], D. Marangotto[8,97], J. Maratas[6,98], J. F. Marchand[61], U. Marconi[57], S. Mariani[19,99], C. Marin Benito[11], M. Marinangeli[27], J. Marks[21], A. M. Marshall[5], P. J. Marshall[3], G. Martellotti[100], L. Martinazzoli[11,54], M. Martinelli[53,54], D. Martinez Santos[4], F. Martinez Vidal[89], A. Massafferri[29], M. Materok[33], R. Matev[11], A. Mathad[2], Z. Mathe[11], V. Matiunin[37], C. Matteuzzi[53], K. R. Mattioli[7], A. Mauri[1], E. Maurice[26], J. Mauricio[13], M. Mazurek[11], M. McCann[30], L. Mcconnell[74], T. H. Mcgrath[14], A. McNab[14], R. McNulty[74], J. V. Mead[3], B. Meadows[9], C. Meaux[25], G. Meier[10], N. Meinert[101], D. Melnychuk[83], S. Meloni[53,54], M. Merk[1,69], A. Merli[8], L. Meyer Garcia[17], M. Mikhasenko[11], D. A. Milanes[102], E. Millard[28], M. Milovanovic[11],

M.-N. Minard[61], A. Minotti[20], L. Minzoni[20,52], S. E. Mitchell[63], B. Mitreska[14], D. S. Mitzel[11], A. Mödden[10], R. A. Mohammed[45], R. D. Moise[30], T. Mombächer[10], I. A. Monroy[102], S. Monteil[6], M. Morandin[40], G. Morello[38], M. J. Morello[34,95], J. Moron[70], A. B. Morris[103], A. G. Morris[28], R. Mountain[23], H. Mu[62], F. Muheim[11,63], M. Mulder[11], D. Müller[11], K. Müller[2], C. H. Murphy[45], D. Murray[14], P. Muzzetto[11,35], P. Naik[5], T. Nakada[27], R. Nandakumar[77], T. Nanut[27], I. Nasteva[17], M. Needham[63], I. Neri[20], N. Neri[8,97], S. Neubert[103], N. Neufeld[11], R. Newcombe[30], T. D. Nguyen[27], C. Nguyen-Mau[27,104], E. M. Niel[18], S. Nieswand[33], N. Nikitin[36], N. S. Nolte[10], C. Nunez[7], A. Oblakowska-Mucha[70], V. Obraztsov[22], D. P. O'Hanlon[5], R. Oldeman[35,71], M. E. Olivares[23], C. J. G. Onderwater[68], A. Ossowska[41], J. M. Otalora Goicochea[17], T. Ovsiannikova[37], P. Owen[2], A. Oyanguren[89], B. Pagare[28], P. R. Pais[11], T. Pajero[45], A. Palano[65], M. Palutan[38], Y. Pan[14], G. Panshin[91], A. Papanestis[77], M. Pappagallo[65,66], L. L. Pappalardo[20,52], C. Pappenheimer[9], W. Parker[49], C. Parkes[14], C. J. Parkinson[4], B. Passalacqua[20], G. Passaleva[19], A. Pastore[65], M. Patel[30], C. Patrignani[57,58], C. J. Pawley[69], A. Pearce[11], A. Pellegrino[1], M. Pepe Altarelli[11], S. Perazzini[57], D. Pereima[37], P. Perret[6], M. Petric[11,12], K. Petridis[5], A. Petrolini[31,81], A. Petrov[96], S. Petrucci[63], M. Petruzzo[8], T. T. H. Pham[23], A. Philippov[24], L. Pica[34,105], M. Piccini[76], B. Pietrzyk[61], G. Pietrzyk[27], M. Pili[45], D. Pinci[100], F. Pisani[11], P. K. Resmi[25], V. Placinta[64], J. Plews[43], M. Plo Casasus[4], F. Polci[39], M. Poli Lener[38], M. Poliakova[23], A. Poluektov[25], N. Polukhina[32,106], I. Polyakov[23], E. Polycarpo[17], G. J. Pomery[5], S. Ponce[11], D. Popov[6,11], S. Popov[24], S. Poslavskii[22], K. Prasanth[41], L. Promberger[11], C. Prouve[4], V. Pugatch[73], H. Pullen[45], G. Punzi[29,105], W. Qian[56], J. Qin[56], R. Quagliani[39], B. Quintana[61], N. V. Raab[74], R. I. Rabadan Trejo[25], B. Rachwal[70], J. H. Rademacker[5], M. Rama[34], M. Ramos Pernas[28], M. S. Rangel[17], F. Ratnikov[24,47], G. Raven[90], M. Reboud[61], F. Redi[27], F. Reiss[14], C. Remon Alepuz[89], Z. Ren[62], V. Renaudin[45], R. Ribatti[34], S. Ricciardi[77], K. Rinnert[3], P. Robbe[18], G. Robertson[63], A. B. Rodrigues[27], E. Rodrigues[3], J. A. Rodriguez Lopez[102], A. Rollings[45], P. Roloff[11], V. Romanovskiy[22], M. Romero Lamas[4], A. Romero Vidal[4], J. D. Roth[7], M. Rotondo[38], M. S. Rudolph[23], T. Ruf[11], J. Ruiz Vidal[89], A. Ryzhikov[47], J. Ryzka[70], J. J. Saborido Silva[4], N. Sagidova[15], N. Sahoo[28], B. Saitta[35,71], M. Salomoni[11], D. Sanchez Gonzalo[13], C. Sanchez Gras[1], R. Santacesaria[100], C. Santamarina Rios[4], M. Santimaria[38], E. Santovetti[59,84], D. Saranin[32], G. Sarpis[12], M. Sarpis[103], A. Sarti[100], C. Satriano[100,107], A. Satta[59], M. Saur[10], D. Savrina[36,37], H. Sazak[6], L. G. Scantlebury Smead[45], S. Schael[33], M. Schellenberg[10], M. Schiller[12], H. Schindler[11], M. Schmelling[108], B. Schmidt[11], O. Schneider[27], A. Schopper[11], M. Schubiger[1], S. Schulte[27], M. H. Schune[18], R. Schwemmer[11], B. Sciascia[38], S. Sellam[4], A. Semennikov[37], M. Senghi Soares[90], A. Sergi[31], N. Serra[2], L. Sestini[40], A. Seuthe[10], P. Seyfert[11], Y. Shang[82], D. M. Shangase[7], M. Shapkin[22], I. Shchemerov[32], L. Shchutska[27], T. Shears[3], L. Shekhtman[48,79], Z. Shen[82], V. Shevchenko[96], E. B. Shields[53,54], E. Shmanin[32], J. D. Shupperd[23], B. G. Siddi[20], R. Silva Coutinho[2], G. Simi[40], S. Simone[65,66], N. Skidmore[14], T. Skwarnicki[23], M. W. Slater[43], I. Slazyk[20,52], J. C. Smallwood[45], J. G. Smeaton[16], A. Smetkina[37], E. Smith[33], M. Smith[30], A. Snoch[1], M. Soares[57], L. Soares Lavra[6], M. D. Sokoloff[9], F. J. P. Soler[12], A. Solovev[15], I. Solovyev[15], F. L. Souza De Almeida[17], B. Souza De Paula[17], B. Spaan[10], E. Spadaro Norella[8,97], P. Spradlin[12], F. Stagni[11], M. Stahl[9], S. Stahl[11], P. Stefko[27], O. Steinkamp[2,32], O. Stenyakin[22], H. Stevens[10], S. Stone[23], M. E. Stramaglia[27], M. Straticiuc[64], D. Strekalina[32], F. Suljik[45], J. Sun[35], L. Sun[42], Y. Sun[49], P. Svihra[14], P. N. Swallow[43], K. Swientek[70], A. Szabelski[83], T. Szumlak[70], M. Szymanski[11], S. Taneja[14], F. Teubert[11], E. Thomas[11], K. A. Thomson[3], V. Tisserand[6], S. T'Jampens[61], M. Tobin[60], L. Tomassetti[20,52], D. Torres Machado[29], D. Y. Tou[39], M. T. Tran[27], E. Trifonova[32], C. Trippl[27], G. Tuci[34,105], A. Tully[27], N. Tuning[1,11], A. Ukleja[83], D. J. Unverzagt[21], E. Ursov[32], A. Usachov[1], A. Ustyuzhanin[24,47], U. Uwer[21], A. Vagner[91], V. Vagnoni[57], A. Valassi[11], G. Valenti[57], N. Valls Canudas[55],

M. van Beuzekom[1], M. Van Dijk[27], E. van Herwijnen[32], C. B. Van Hulse[74], M. van Veghel[68], R. Vazquez Gomez[4], P. Vazquez Regueiro[4], C. Vázquez Sierra[11], S. Vecchi[20], J. J. Velthuis[5], M. Veltri[19,109], A. Venkateswaran[23], M. Veronesi[1], M. Vesterinen[28], D. Vieira[9], M. Vieites Diaz[27], H. Viemann[101], X. Vilasis-Cardona[55], E. Vilella Figueras[3], P. Vincent[39], D. Vom Bruch[25], A. Vorobyev[15], V. Vorobyev[48,79], N. Voropaev[15], R. Waldi[101], J. Walsh[34], C. Wang[21], J. Wang[82], J. Wang[60], J. Wang[62], J. Wang[42], M. Wang[62], R. Wang[5], Y. Wang[87], Z. Wang[2], Z. Wang[62], H. M. Wark[3], N. K. Watson[43], S. G. Weber[39], D. Websdale[30], C. Weisser[46], B. D. C. Westhenry[5], D. J. White[14], M. Whitehead[5], D. Wiedner[10], G. Wilkinson[45], M. Wilkinson[23], I. Williams[16], M. Williams[46], M. R. J. Williams[63], F. F. Wilson[77], W. Wislicki[83], M. Witek[41], L. Witola[21], G. Wormser[18], S. A. Wotton[16], H. Wu[23], K. Wyllie[11], Z. Xiang[56], D. Xiao[87], Y. Xie[87], A. Xu[82], J. Xu[56], L. Xu[62], M. Xu[87], Q. Xu[56], Z. Xu[82], Z. Xu[56], D. Yang[62], S. Yang[56], Y. Yang[56], Z. Yang[62], Z. Yang[49], Y. Yao[23], L. E. Yeomans[3], H. Yin[87], J. Yu[110], X. Yuan[23], O. Yushchenko[22], E. Zaffaroni[27], M. Zavertyaev[106,108], M. Zdybal[41], O. Zenaiev[11], M. Zeng[62], D. Zhang[87], L. Zhang[62], S. Zhang[82], Y. Zhang[82], Y. Zhang[45], A. Zhelezov[21], Y. Zheng[56], X. Zhou[56], Y. Zhou[56], X. Zhu[62], Z. Zhu[56], V. Zhukov[33,36], J. B. Zonneveld[63], Q. Zou[60], S. Zucchelli[57,58], D. Zuliani[40] and G. Zunica[14]

[1]Nikhef National Institute for Subatomic Physics, Amsterdam, Netherlands. [2]Physik-Institut, Universität Zürich, Zürich, Switzerland. [3]Oliver Lodge Laboratory, University of Liverpool, Liverpool, UK. [4]Instituto Galego de Física de Altas Enerxías (IGFAE), Universidade de Santiago de Compostela, Santiago de Compostela, Spain. [5]H.H. Wills Physics Laboratory, University of Bristol, Bristol, UK. [6]Université Clermont Auvergne, CNRS/IN2P3, LPC, Clermont-Ferrand, MI, France. [7]University of Michigan, Ann Arbor, USA. [8]INFN Sezione di Milano, Milano, Italy. [9]University of Cincinnati, Cincinnati, OH, USA. [10]Fakultät Physik, Technische Universität Dortmund, Dortmund, Germany. [11]European Organization for Nuclear Research (CERN), Geneva, Switzerland. [12]School of Physics and Astronomy, University of Glasgow, Glasgow, UK. [13]ICCUB, Universitat de Barcelona, Barcelona, Spain. [14]Department of Physics and Astronomy, University of Manchester, Manchester, UK. [15]Petersburg Nuclear Physics Institute NRC Kurchatov Institute (PNPI NRC KI), Gatchina, Russia. [16]Cavendish Laboratory, University of Cambridge, Cambridge, UK. [17]Universidade Federal do Rio de Janeiro (UFRJ), Rio de Janeiro, Brazil. [18]Université Paris-Saclay, CNRS/IN2P3, IJCLab, Orsay, France. [19]INFN Sezione di Firenze, Firenze, Italy. [20]INFN Sezione di Ferrara, Ferrara, Italy. [21]Physikalisches Institut, Ruprecht-Karls-Universität Heidelberg, Heidelberg, Germany. [22]Institute for High Energy Physics NRC Kurchatov Institute (IHEP NRC KI), Protvino, Russia. [23]Syracuse University, Syracuse, NY, USA. [24]Yandex School of Data Analysis, Moscow, Russia. [25]Aix Marseille Univ, CNRS/IN2P3, CPPM, Marseille, France. [26]Laboratoire Leprince-Ringuet, CNRS/IN2P3, Ecole Polytechnique, Institut Polytechnique de Paris, Palaiseau, France. [27]Institute of Physics, Ecole Polytechnique Fédérale de Lausanne (EPFL), Lausanne, Switzerland. [28]Department of Physics, University of Warwick, Coventry, UK. [29]Centro Brasileiro de Pesquisas Físicas (CBPF), Rio de Janeiro, Brazil. [30]Imperial College London, London, UK. [31]INFN Sezione di Genova, Genova, Italy. [32]National University of Science and Technology 'MISIS', Moscow, Russia. [33]I. Physikalisches Institut, RWTH Aachen University, Aachen, Germany. [34]INFN Sezione di Pisa, Pisa, Italy. [35]INFN Sezione di Cagliari, Monserrato, Italy. [36]Institute of Nuclear Physics, Moscow State University (SINP MSU), Moscow, Russia. [37]Institute of Theoretical and Experimental Physics NRC Kurchatov Institute (ITEP NRC KI), Moscow, Russia. [38]INFN Laboratori Nazionali di Frascati, Frascati, Italy. [39]LPNHE, Sorbonne Université, Paris Diderot Sorbonne Paris Cité, CNRS/IN2P3, Paris, France. [40]Universita degli Studi di Padova, Universita e INFN, Padova, Padova, Italy. [41]Henryk Niewodniczanski Institute of Nuclear Physics Polish Academy of Sciences, Kraków, Poland. [42]School of Physics and Technology, Wuhan University, Wuhan, China. [43]University of Birmingham, Birmingham, UK. [44]Università di Modena e Reggio Emilia, Modena, Italy. [45]Department of Physics, University of Oxford, Oxford, UK. [46]Massachusetts Institute of Technology, Cambridge, MA, USA. [47]National Research University Higher School of Economics, Moscow, Russia. [48]Budker Institute of Nuclear Physics (SB RAS), Novosibirsk, Russia. [49]University of Maryland, College Park, MD, USA. [50]Guangdong Provencial Key Laboratory of Nuclear Science, Institute of Quantum Matter, South China Normal University, Guangzhou, China. [51]Institute for Nuclear Research of the Russian Academy of Sciences (INR RAS), Moscow, Russia. [52]Università di Ferrara, Ferrara, Italy. [53]INFN Sezione di Milano-Bicocca, Milano, Italy. [54]Università di Milano Bicocca, Milano, Italy. [55]DS4DS, La Salle, Universitat Ramon Llull, Barcelona, Spain. [56]University of Chinese Academy of Sciences, Beijing, China. [57]INFN Sezione di Bologna, Bologna, Italy. [58]Università di Bologna, Bologna, Italy. [59]INFN Sezione di Roma Tor Vergata, Roma, Italy. [60]Institute Of High Energy Physics (IHEP), Beijing, China. [61]Univ. Savoie Mont Blanc, CNRS, IN2P3-LAPP, Annecy, France. [62]Center for High Energy Physics, Tsinghua University, Beijing, China. [63]School of Physics and Astronomy, University of Edinburgh, Edinburgh, UK. [64]Horia Hulubei National Institute of Physics and Nuclear Engineering, Bucharest-Magurele, Romania. [65]INFN Sezione di Bari, Bari, Italy. [66]Università di Bari, Bari, Italy. [67]Los Alamos National Laboratory (LANL), Los Alamos, NM, USA. [68]Van Swinderen Institute, University of Groningen, Groningen, Netherlands. [69]Universiteit Maastricht, Maastricht, Netherlands. [70]Faculty of Physics and Applied Computer Science, AGH University of Science and Technology, Kraków, Poland. [71]Università di Cagliari, Cagliari, Italy. [72]Eotvos Lorand University, Budapest, Hungary. [73]Institute for Nuclear Research of the National Academy of Sciences (KINR), Kyiv, Ukraine. [74]School of Physics, University College Dublin, Dublin, Ireland. [75]NSC Kharkiv Institute of Physics and Technology (NSC KIPT), Kharkiv, Ukraine. [76]INFN Sezione di Perugia, Perugia, Italy. [77]STFC Rutherford Appleton Laboratory, Didcot, UK. [78]School of Physics and Astronomy, Monash University, Melbourne, Victoria, Australia. [79]Novosibirsk State University, Novosibirsk, Russia. [80]Department of Physics and Astronomy, Uppsala University, Uppsala, Sweden. [81]Università di Genova, Genova, Italy. [82]School of Physics State Key Laboratory of Nuclear Physics and Technology, Peking University, Beijing, China. [83]National Center for Nuclear Research (NCBJ), Warsaw, Poland. [84]Università di Roma Tor Vergata, Roma, Italy. [85]Pontifícia Universidade Católica do Rio de Janeiro (PUC-Rio), Rio de Janeiro, Brazil. [86]Universidade Federal do Triângulo Mineiro (UFTM), Uberaba-MG, Brazil. [87]Institute of Particle Physics, Central China Normal University, Wuhan, China. [88]Hangzhou Institute for Advanced Study, UCAS, Hangzhou, China. [89]Instituto de Fisica Corpuscular, Centro Mixto Universidad de Valencia - CSIC, Valencia, Spain. [90]Nikhef National Institute for Subatomic Physics and VU University Amsterdam, Amsterdam, Netherlands. [91]National Research Tomsk Polytechnic University, Tomsk, Russia. [92]Faculty of Computer Science, Electronics and Telecommunications, AGH University of Science and Technology, Kraków, Poland. [93]Università di Siena, Siena, Italy. [94]Università di Padova, Padova, Italy. [95]Scuola Normale Superiore, Pisa, Italy. [96]National Research Centre Kurchatov Institute, Moscow, Russia. [97]Università degli Studi di

Milano, Milano, Italy. [98]MSU–Iligan Institute of Technology (MSU-IIT), Iligan, Philippines. [99]Università di Firenze, Firenze, Italy. [100]INFN Sezione di Roma La Sapienza, Roma, Italy. [101]Institut für Physik, Universität Rostock, Rostock, Germany. [102]Departamento de Fisica, Universidad Nacional de Colombia, Bogota, Colombia. [103]Universität Bonn Helmholtz-Institut für Strahlen und Kernphysik, Bonn, Germany. [104]Hanoi University of Science, Hanoi, Vietnam. [105]Università di Pisa, Pisa, Italy. [106]P.N. Lebedev Physical Institute, Russian Academy of Sciences (LPI RAS), Moscow, Russia. [107]Università della Basilicata, Potenza, Italy. [108]Max-Planck-Institut für Kernphysik (MPIK), Heidelberg, Germany. [109]Università di Urbino, Urbino, Italy. [110]Physics and Micro Electronic College, Hunan University, Changsha City, China. ✉e-mail: alessandro.bertolin@pd.infn.it

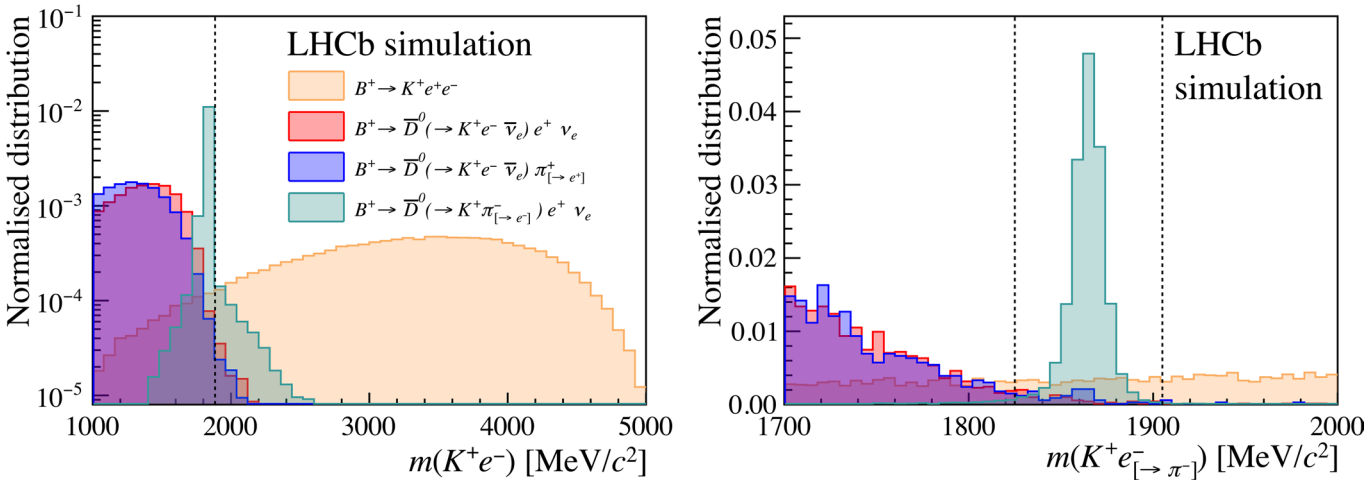

Extended Data Fig. 1 | Simulated K^+e^- mass distributions for signal and various cascade background samples. The signal is represented by the orange shaded region and the various cascade background contributions by red, dark blue and light blue shaded regions. The distributions are all normalised to unity. (Left, with log *y*-scale) the bremsstrahlung correction to the momentum of the electron is applied, resulting in a tail to the right. The region to the left of the vertical dashed line is rejected. (Right, with linear *y*-scale) the mass is computed only from the track information. The notation $\pi^-_{[\to e^-]}$ ($e^-_{[\to \pi^-]}$) is used to denote an pion (electron) that is reconstructed as an electron (pion). The region between the dashed vertical lines is rejected.

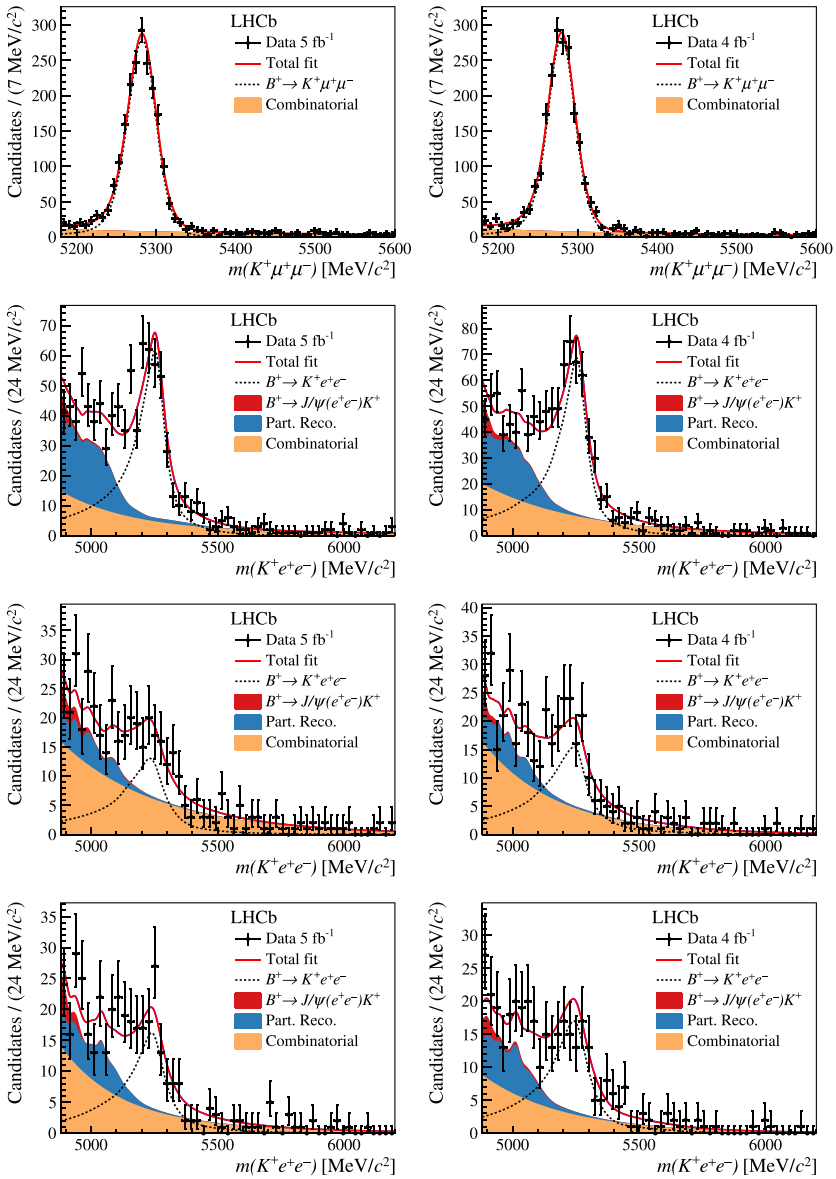

Extended Data Fig. 2 | Nonresonant candidates invariant mass distributions. Distribution of the invariant mass $m(K^+\ell^+\ell^-)$ for nonresonant candidates in the (left) sample previously analysed[11] and (right) the new data sample. The top row shows the fit to the muon modes and the subsequent rows the fits to the electron modes triggered by (second row) one of the electrons, (third row) the kaon and (last row) by other particles in the event. The fit projections are superimposed, with dotted lines describing the signal contribution and solid areas representing each of the background components described in the text and listed in the legend. Uncertainties on the data points are statistical only and represent one standard deviation, calculated assuming Poisson-distributed entries. The y-axis in each figure shows the number of candidates in an interval of the indicated width.

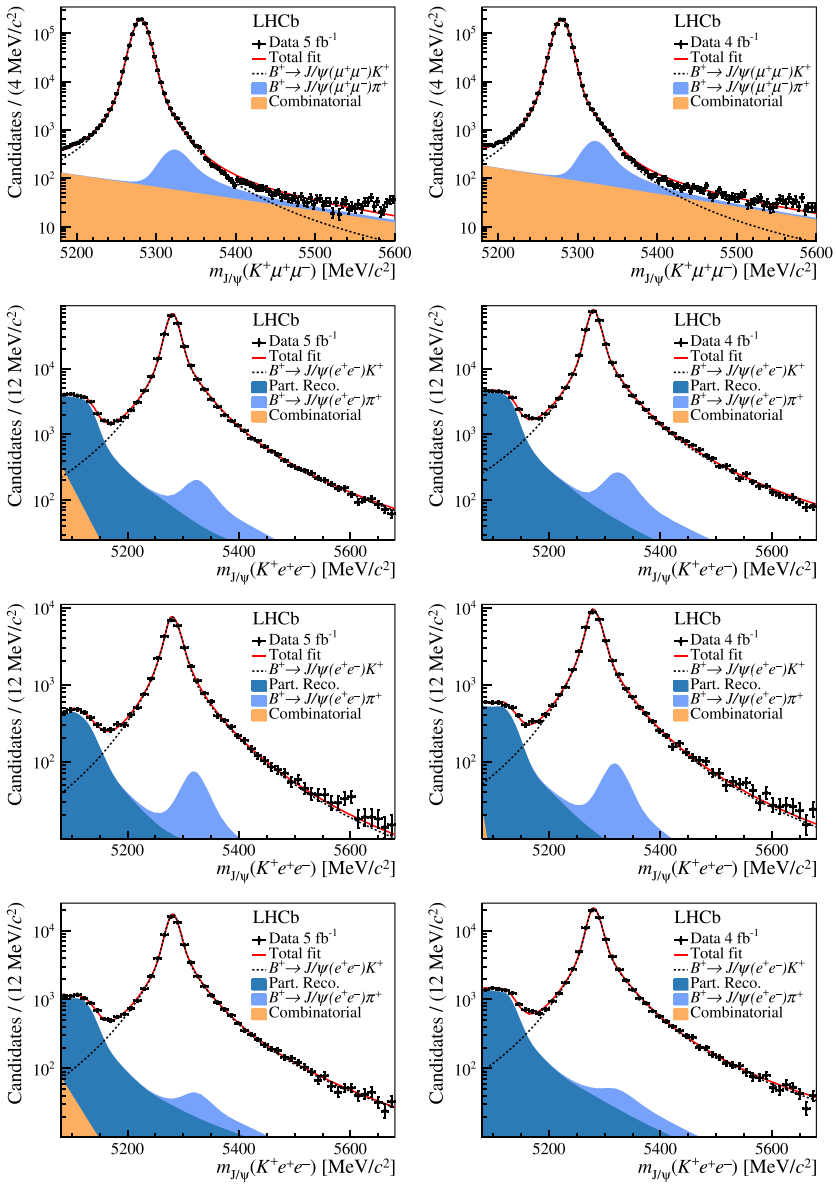

Extended Data Fig. 3 | Resonant candidates invariant mass distributions. Distribution of the invariant mass $m_{J/\psi}(K^+\ell^+\ell^-)$ for resonant candidates in the (left) sample previously analysed[11] and (right) the new data sample. The top row shows the fit to the muon modes and the subsequent rows the fits to the electron modes triggered by (second row) one of the electrons, (third row) the kaon and (last row) by other particles in the event. The fit projections are superimposed, with dotted lines describing the signal contribution and solid areas representing each of the background components described in the text and listed in the legend. Uncertainties on the data points are statistical only and represent one standard deviation, calculated assuming Poisson-distributed entries. The y-axis in each figure shows the number of candidates in an interval of the indicated width.

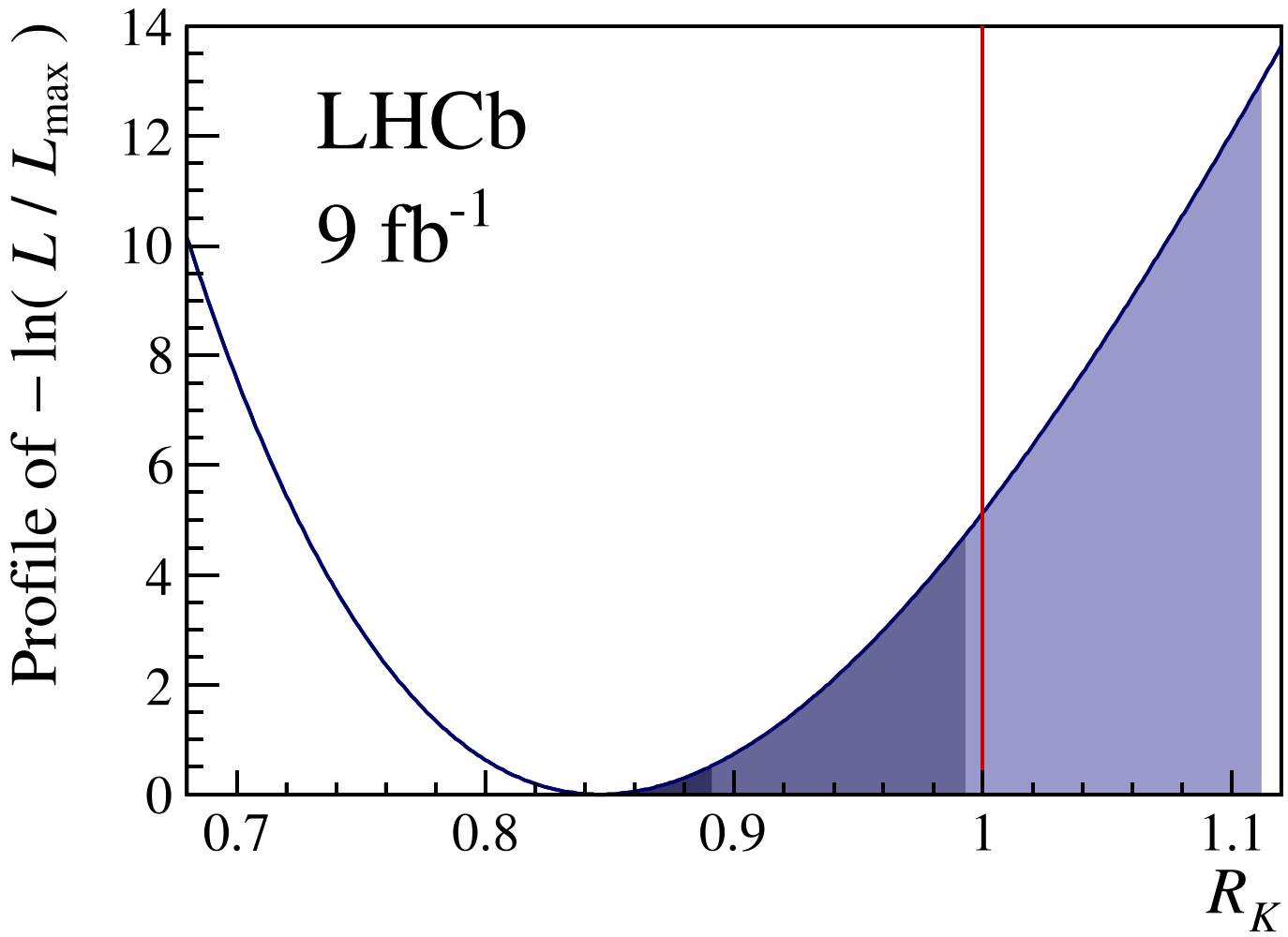

Extended Data Fig. 4 | Likelihood function from the fit to the nonresonant $B^+ \to K^+ \ell^+ \ell^-$ candidates. Ratio between the likelihood value (L) and that found by the fit (L_{max}) as a function of R_K. The extent of the dark, medium and light blue regions shows the values allowed for R_K at 1σ, 3σ and 5σ levels. The red line indicates the prediction from the SM.

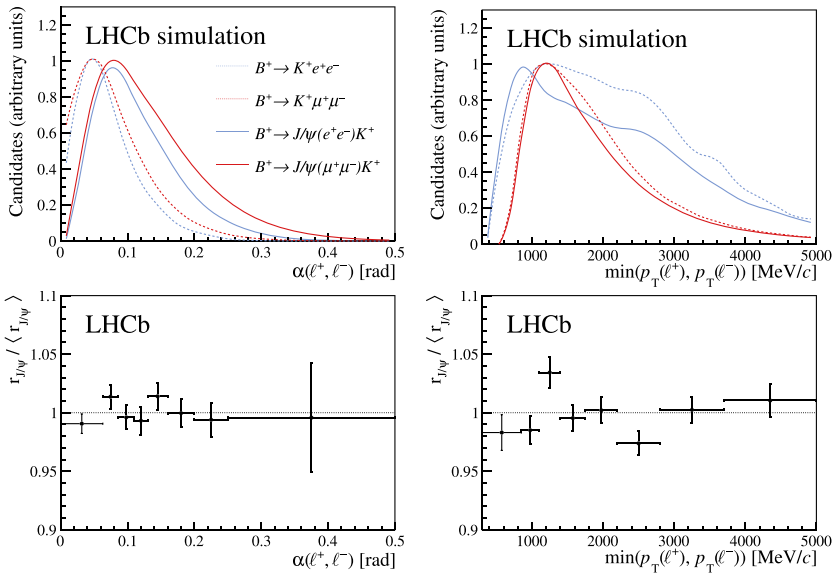

Extended Data Fig. 5 | Differential $r_{J/\psi}$ measurement. (Top) distributions of the reconstructed spectra of (left) the angle between the leptons, $\alpha(\ell^+, \ell^-)$, and (right) the minimum p_T of the leptons for $B^+ \to K^+\ell^+\ell^-$ and $B^+ \to J/\psi(\to \ell^+\ell^-)K^+$ decays. (Bottom) the single ratio $r_{J/\psi}$ relative to its average value $< r_{J/\psi} >$ as a function of these variables. In the electron minimum p_T spectra, the structure at 2800 MeV/c is related to the trigger threshold. Uncertainties on the data points are statistical only and represent one standard deviation.

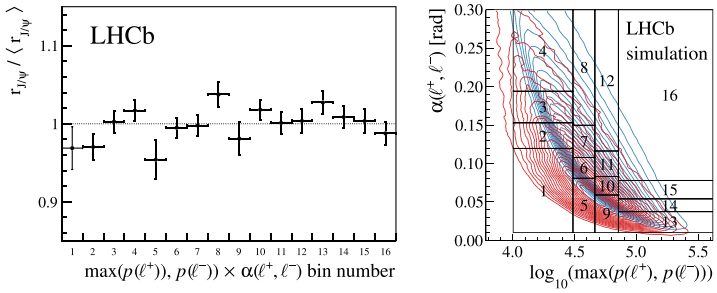

Extended Data Fig. 6 | Double differential $r_{J/\psi}$ measurement. (Left) the value of $r_{J/\psi}$ relative to the average value of $r_{J/\psi}$ measured in two-dimensional bins of the maximum lepton momentum, $p(\ell)$, and the opening angle between the two leptons, $\alpha(\ell^+, \ell^-)$. (Right) the bin definition in this two-dimensional space together with the distribution for $B^+ \to K^+e^+e^-$ ($B^+ \to J/\psi(\to e^+e^-)K^+$) decays depicted as red (blue) contours. Uncertainties on the data points are statistical only and represent one standard deviation.

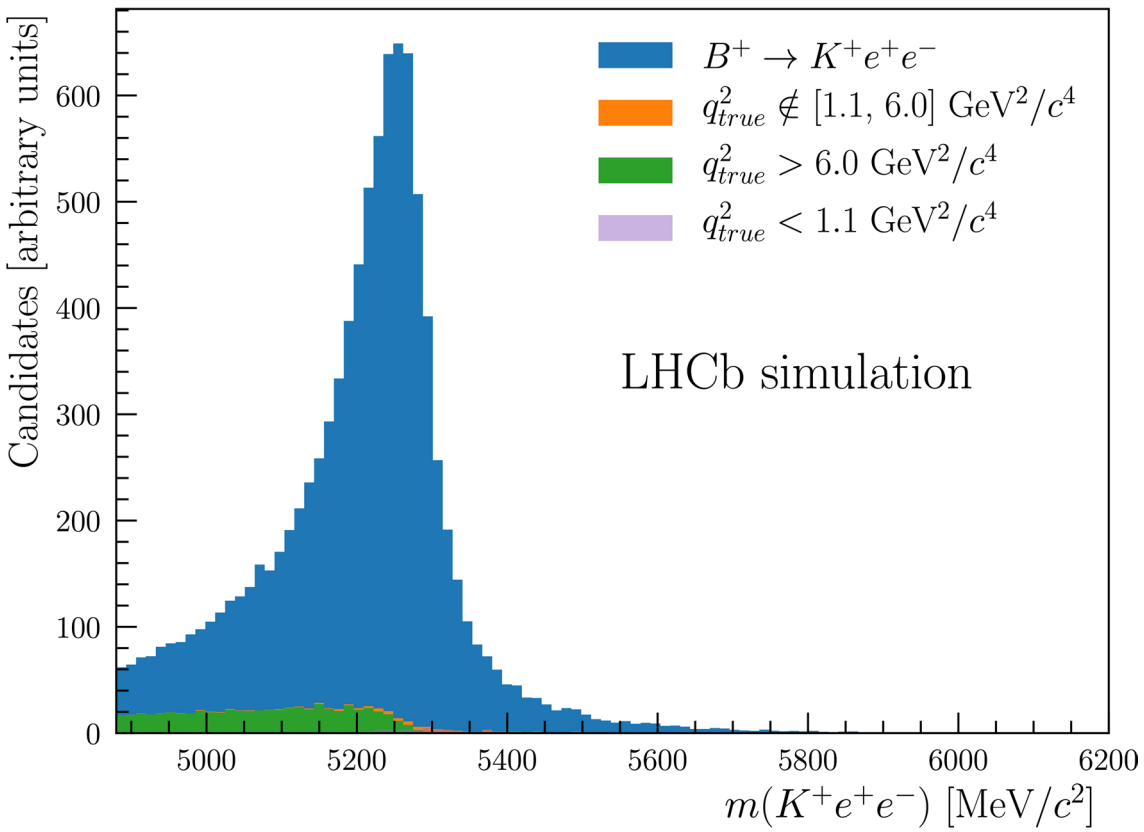

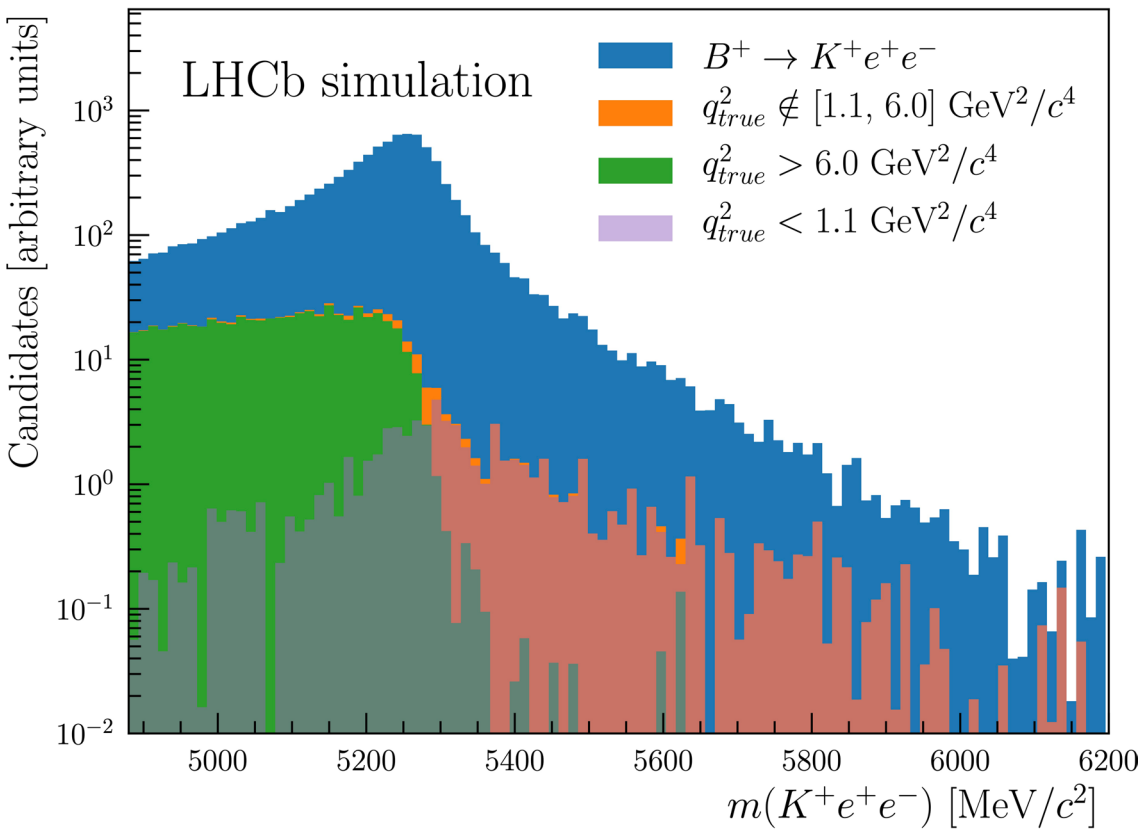

Extended Data Fig. 7 | See next page for caption.

Extended Data Fig. 7 | Distribution of $m(K^+e^+e^-)$ in simulated $B^+ \to K^+e^+e^-$ decays. Distribution of $m(K^+e^+e^-)$ in simulated $B^+ \to K^+e^+e^-$ decays. The orange shaded area corresponds to $B^+ \to K^+e^+e^-$ candidates with true q^2 (q^2_{true}) outside the [1.1, 6.0] GeV $^2/c^4$ interval. The green and purple components correspond to candidates with $q^2_{true} > 6.0$ GeV $^2/c^4$ and $q^2_{true} < 1.1$ GeV $^2/c^4$, respectively. Linear (top) and logarithmic (bottom) scales are shown.

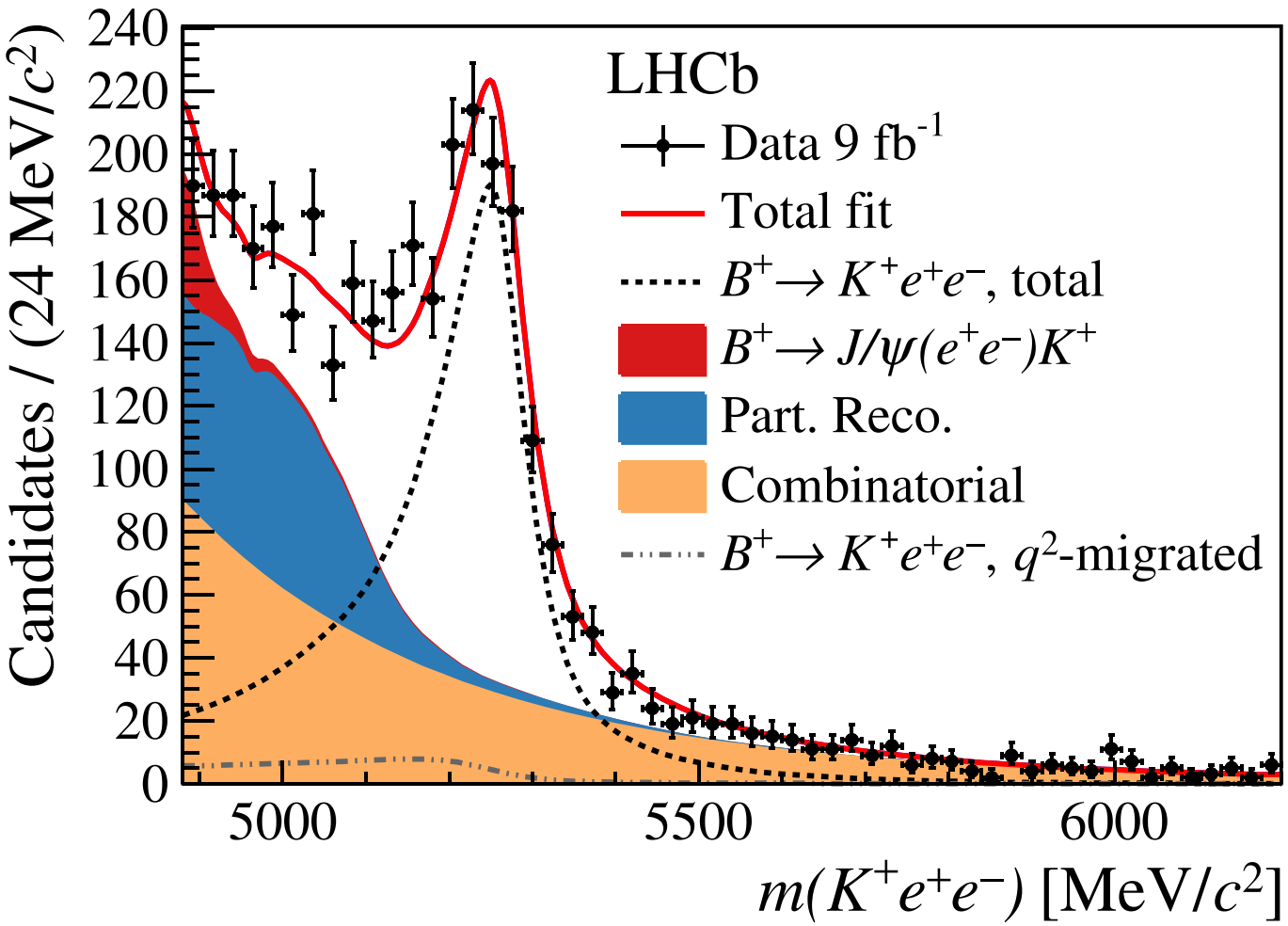

Extended Data Fig. 8 | Candidate invariant mass distributions. Distribution of the invariant mass $m(K^+e^+e^-)$ for $B^+ \to K^+e^+e^-$ candidates. The fit projection is superimposed, with a black dotted line describing the signal contribution and solid areas representing each of the background components described in the text and listed in the legend. For illustration, the expected distribution of signal candidates with true q^2 outside the interval $[1.1, 6.0]\text{GeV}^2/c^4$ is shown as a grey dashed and dotted line. Uncertainties on the data points are statistical only and represent one standard deviation, calculated assuming Poisson-distributed entries. The y-axis in each figure shows the number of candidates in an interval of the indicated width.

Decay mode	q^2 $[\mathrm{GeV}^2/c^4]$	$m_{(J/\psi)}(K^+\ell^+\ell^-)$ $[\mathrm{GeV}/c^2]$
nonresonant e^+e^-	1.1 – 6.0	4.88 – 6.20
resonant e^+e^-	6.00 – 12.96	5.08 – 5.70
nonresonant $\mu^+\mu^-$	1.1 – 6.0	5.18 – 5.60
resonant $\mu^+\mu^-$	8.68 – 10.09	5.18 – 5.60

Extended Data Table 1 | Nonresonant and resonant mode q^2 and $m(K^+\ell^+\ell^-)$ ranges. The variables $m(K^+\ell^+\ell^-)$ and $m_{J/\psi}(K^+\ell^+\ell^-)$ are used for nonresonant and resonant decays, respectively.

Decay mode	Yield
$B^+ \to K^+e^+e^-$	$1\,640 \pm 70$
$B^+ \to K^+/mu^+\mu^-$	$3\,850 \pm 70$
$B^+ \to J/\psi(\to e^+e^-)K^+$	$743\,300 \pm 900$
$B^+ \to J/\psi(\to \mu^+\mu^-)K^+$	$2\,288\,500 \pm 1\,500$

Extended Data Table 2 | Yields of the nonresonant and resonant decay modes. Yields of the nonresonant and resonant decay modes obtained from the fits to the data. The quoted uncertainty is the combination of statistical and systematic effects.